Title

Probing the high-pressure densification of amorphous silica nanomaterials using SBA-15: An investigation into the paradoxical nature of the first sharp diffraction peak

Authors

Bull, Michael R

Huber, Rachel C

Yu, Ping

et al.

Publication Date

2025-05-01

DOI

10.1016/j.jnoncrysol.2025.123448

Probing the High-Pressure Densification of Amorphous Silica Nanomaterials using SBA-15: an Investigation into the Paradoxical Nature of the First Sharp Diffraction Peak

Authors: Michael R. Bull (UCD)[ab], Rachel C. Huber (LANL)[c], Ping Yu (UCD)[d], Tanner J Finney (LANL)[e], Noah Felvey (UCD)[a], Paul Chow (ANL)[f], Yuming Xiao (ANL)[f], Tonya L. Kuhl (UCD)[a], Erik B. Watkins (LANL now ORNL)[eg*]

[a]Department of Chemical Engineering, University of California Davis, CA 95616, USA

[b]High Explosive Science and Technology (Q-5), Los Alamos National Laboratory, Los Alamos, NM 87545, USA

[c]Dynamic Experiments Division, Los Alamos National Laboratory, Los Alamos, NM 87545, USA

[d]Nuclear Magnetic Resonance Facility, University of California, Davis, CA 95616, USA

[e]MPA-11, Materials Physics and Applications Division, Los Alamos National Laboratory, Los Alamos, NM 87545, USA

[f]HPCAT, X-Ray Science Division, Argonne National Laboratory, Argonne, IL 60439, USA

[g]Neutron Scattering Division, Oak Ridge National Laboratory, Oak Ridge, TN 37831, USA

Corresponding Author Details:

Erik Watkins (watkinseb@ornl.gov), 1 Bethel Valley Road, Bldg 8600 MS-6475, Oak Ridge, TN 37830-6475

Probing the High-Pressure Densification of Amorphous Silica Nanomaterials using SBA-15: an Investigation into the Paradoxical Nature of the First Sharp Diffraction Peak

Abstract

The densification and X-ray scattering of mesoporous silica (SBA-15) were measured simultaneously under gigapascal (GPa) pressures. The results are compared to previous work on amorphous silica (*a*SiO_2) and demonstrate the feasibility of measuring the densification of *a*SiO_2 nanomaterials with small angle X-ray scattering (SAXS) in-situ in a diamond anvil cell. Compared to fused silica, the position of the SBA-15 first sharp diffraction peak (FSDP) is 7 times more sensitive to pressure and has a transition in its pressure dependance at a lower pressure (~2 GPa vs. ~13 GPa). SBA-15 has two densification regimes, low-density amorphous and high-density amorphous, which have equations of state comparable to low-density amorphous and high-density amorphous fused silica. The transition between these two regimes occurs at a lower pressure than for fused silica (~1.5 GPa vs. ~13 GPa). The results suggest that there is no direct relationship between the FSDP position and the *a*SiO_2 density during compression.

Keywords: Amorphous Silica, Mesoporous Silica, Diamond Anvil Cell, First Sharp Diffraction Peak, Equation of State, Small Angle X-ray Scattering

Highlights

- SBA-15, a type of nanoscale *a*SiO_2, is hydrostatically compressed up to ~5 GPa.
- Equation of state and microstructural changes are probed in-situ using SAXS and WAXS.
- SBA-15 transitions from a low-density amorphous to a high-density amorphous EOS at low pressure and density.
- SBA-15's First Sharp Diffraction Peak is more pressure sensitive than other amorphous silica polyamorphs.
- *a*SiO_2 bulk modulus is shown to not be coupled with the FSDP pressure-sensitivity.

Inspec Classification Codes

A60, A90

1.0 Introduction

Amorphous silica (aSiO$_2$) is the archetypal model material for high pressure glass studies due to its ubiquity, chemical simplicity, and relevance to both geological and industrial systems. Current high pressure (>1 GPa) studies on aSiO$_2$ focus on melt-derived polyamorphs, e.g. fused silica, densified fused silica, and vitreous silica. However, aSiO$_2$ consists of a much wider family of polyamorphs. One important subset is mesoporous silicas, commonly used for catalysis and environmental adsorption due to their high surface area. This work studies the high-pressure behavior of the periodic mesoporous silica SBA-15 using a diamond anvil cell (DAC) and in-situ X-ray scattering.

The molecular structure of aSiO$_2$ is a polymerized three-dimensional (3D) network of SiO$_4$ tetrahedra [1]. Short-range order, at length scales below ~2 Å, comes from bonding within these tetrahedra. The tetrahedra interconnect through bridging oxygens, forming a continuous network characterized by ring structures of various sizes [2]. The rings, while not regularly shaped, are all of fairly similar structure [3,4]. This regularity gives rise to structural ordering at intermediate length scales (~5 – 50 Å), referred to as intermediate range order (IRO) [1]. The microstructures comprising the IRO include rings, network cages formed by multiple rings, and hypothesized structures such as pseudo-Bragg planes [5]. The IRO structures are reflected in diffraction features such as the first sharp diffraction peak (FSDP).

The FSDP is a common, but largely qualitative, measure of change in the IRO with spatial correlations between ~4 – 10 Å [5]. Many theories have been proposed regarding its structural origins, and there is significant controversy over which (if any) are correct [4–9]. Its position, intensity, and width are all highly sensitive to pressure [10–12]. The main structural differences between aSiO$_2$ polyamorphs lie in the IRO, making the FSDP a useful marker for comparisons between them [13–15].

Amorphous-amorphous microstructural transitions are common during compression of glasses. These transitions are typically denoted by changes in density, i.e. going from a low-density amorphous (LDA) regime to a high-density amorphous (HDA) regime. The LDA and HDA mechanical properties and atomic structure can differ significantly, just as for crystalline polymorphs. The compressive behavior of both regimes can be quantified using equations of state (EOS), which describe the relationship between pressure and volume. Although most amorphous-amorphous transitions involve changing atomic coordination numbers, aSiO$_2$ is a special case that can have a stable HDA state at pressures below those required to increase the coordination number [16,17].

We investigate SBA-15 under hydrostatic compression at room temperature (cold compression) up to ~5 GPa and under uniaxial (non-hydrostatic) compression up to ~1.2 GPa using a diamond anvil cell (DAC) and in-situ synchrotron X-ray scattering.

SBA-15 is one of the most studied mesoporous silicas and is synthesized by molding a TEOS-based silicate gel around a surfactant template [18–21]. The gel is then heated to perform a condensation reaction and to burn out any remaining surfactants. After heating almost all organic groups are eliminated (except for a large number of hydroxyl defects) [22]. The resulting material is a glass powder composed of few-micron sized, elongated particles (aka grains). Each particle is a highly porous form of aSiO$_2$. The pore structure is dominated by ~10 nm diameter mesopores that form a two-dimensional (2D) hexagonal array (*P*6*mm* mesolattice), with nanoscale aSiO$_2$ walls surrounding them (Fig. 1) [23]. Embedded within the aSiO$_2$ walls is a significant volume of both complementary pores forming “holes” between the primary mesopores and of micropores surrounding the mesopores in a “corona” [24–27]. It was previously found that ~53% of the porosity volume in SBA-15 comes from the primary, ordered mesopores, and the remaining ~47% comes from the complementary pores and micropores [25]. Thus, SBA-15 has a high degree of interconnectivity between the mesopores via irregular nano-scale channels. Despite micron-scale particle diameters, SBA-15 is a nanoscale material due to its high surface area to volume ratio and few-nanometer thin walls.

[Insert Figure 1 here]

The aSiO$_2$ in the walls of SBA-15 shares a similar microstructure with fused silica, largely because the IRO structure must be similar for glasses of the same chemistry due to similar intertetrahedral ring sizes/shapes, cation nearest neighbor distances, and intertetrahedral bond angles. Both SBA-15 and fused silica have a fully polymerized bulk intertetrahedral network (see SI Section 1.5), identical Si-O bond angles and distances, and similar O-O and Si-Si nearest neighbor distances [5,15,28]. However, SBA-15 also has several microstructural differences with fused silica due to its larger skeletal density, different synthesis route, and nanoscale dimensions. SBA-15 has a higher proportion of Q2 and Q3 species due to its large surface area (for further details, see SI Section 1.5), and of small 3- and 4-membered intertetrahedral rings [29]. The SBA-15 FSDP peak typically has a weaker intensity, a larger full width half maximum (FWHM), and a higher momentum transfer, q, position than fused silica [15,22,30,31]. Differences in their IROs are observed (via the pair distribution function) beyond a correlation length of ~3.5 Å [28].

Previous studies of mesoporous silicas using DACs have reported significantly different bulk moduli (ranging from 5 – 47 GPa), likely attributable to disparities in pressure conditions (either hydrostatic or quasi-hydrostatic) [32–34]. These previous studies lacked the densification datapoint density and signal-to-noise ratio to rigorously model a pressure dependent EOS. In addition to mesoporous silicas, fumed silica nanoparticles

have also been studied with DACs. Fumed silica is another *a*SiO_2 nanomaterial made from a reactive Si precursor and in many ways is similar to SBA-15: due to its high surface area fumed silica has a higher proportion of Q2 and Q3 species [35] and more 3- and 4-membered rings [29,36,37] than fused silica. However, fumed silica's density, ambient pressure FSDP position, and IRO (via the pair distribution function) are all dissimilar to SBA-15 and more like that of fused silica [13,37]. Notably, the FSDP of fumed silica [13] exhibits greater sensitivity to pressure than that of fused silica or almost any other type of *a*SiO_2 [16,38].

2.0 Materials and methods

2.1 Materials and material property measurements

SBA-15 was purchased from ACS Materials (synthesized via the hydrothermal method with Pluronic 123 as the surfactant template and TEOS as the silicon source, then calcined in air at 550°C for 6 hours). The material properties at ambient pressure (1 atm) and room temperature were studied using the following techniques: ^{29}Si MAS NMR (Bruker 500 MHz AVANCE) was used to measure the Q species and degree of polymerization. A nitrogen gas adsorption analyzer (Micrometric 3Flex Adsorption Analyzer) was used to measure the specific surface area, pore volume, and mesopore diameter. Helium pycnometry (Anton Paar Ultrapyc 5000 Micro) was used to measure the SBA-15 skeletal density. The tapping method was used to measure bulk powder density. Further details on material property measurements and a table of results are given in SI Section 1.

2.2 X-ray scattering measurements

Small angle X-ray scattering (SAXS) and wide angle X-ray scattering (WAXS) measurements were carried out at Argonne National Laboratory's Advanced Photon Source (APS) at HP-CAT (beamline 16-ID-D) using 20 keV monochromatic X-rays (λ=0.6199 Å). Pt and Rh KB mirrors removed higher energy harmonics and focused the x-ray beam to ~25 × 25 μm (FWHM) at the sample position and ~500 × 500 μm (FWHM) at the SAXS detector position. All WAXS and SAXS data were measured in-situ in the diamond anvil cell (DAC).

The DAC delivered hydrostatic and uniaxial pressures for sample compression [39]. The hydrostatic measurements used a pressure-transmitting medium (PTM) of 4:1 methanol ethanol (hydrostatic up to 10 GPa [40]) and the non-hydrostatic (uniaxial) measurements used ambient air. The DAC was a symmetric design using type II diamonds, 300 μm

diameter culets, and a stainless-steel gasket. The sample chamber was ~100 μm in diameter and ~100 – 250 μm thick (at ambient conditions).

WAXS data was collected on a Pilatus 100K detector, offset to let the SAXS beam pass, and located ~170 mm from the sample to capture a momentum transfer of $1.4 < q < 4.0$ Å^{-1} with azimuthal coverage of ~40 – 120°. WAXS data was calibrated using a gold standard and radially integrated to 1D WAXS patterns using DIOPTAS [41]. Reported WAXS and SAXS intensities are not on an absolute scale but are self-consistent across our measurements.

SAXS data was collected using a MAR345 detector (345 mm diameter active area) located ~3050 mm from the sample. To minimize air scattering, the SAXS beam was passed through an He-filled container with X-ray transparent windows: a 50 μm thick mica window upstream and a 17 μm thick Kapton window downstream. A beam stop immediately upstream of the Kapton window shielded the detector from the direct beam and intense low-q scattering. Due to limitations in the dynamic range of the MAR345 detector, SAXS data was collected in two measurements with overlapping q ranges. The low-q configuration used a 2 mm diameter tungsten rod for the beam stop and measured data between $0.0025 < q < 0.05$ Å^{-1}. The high-q configuration used the tungsten rod and a U.S. dime (17.91 mm diameter 91.7 wt% Cu, 8.3 wt% Ni) for the beam stop and measured data between $0.03 < q < 0.5$ Å^{-1}. Artifacts from intense diamond scattering limited the useful low-q range to $q > 0.0045$ Å^{-1}. Background measurements through a fully assembled DAC without a sample or PTM were used to quantify instrument specific scattering signals. The background limited the useful high-q range to $q < 0.15$ Å^{-1}. SAXS data was calibrated using diffraction from a silver behenate standard. 1D SAXS patterns, in arbitrary units of intensity, were calculated by applying a dark field correction and subtracting the instrument specific scattering from the detector images, radially integrating the corrected images, and scaling the high- and low-q measurements to each other in the overlap region.

For fitting SAXS and WAXS data, the systematic error σ_I in Poisson counting statistics (intensity I) was estimated $\sigma_I = \sqrt{I} + (0.05 * I)$ and factored into fits as $weight = 1/\sigma_I^2$. All fitting used least squares regression (trust-region method) in MATLAB with intensity weights factored into the fits. The error in fitted parameters was taken as half of the 95% confidence interval, equivalent to one standard deviation.

3.0 Theory and modelling for hydrostatic compression

3.1 SAXS modelling

Modelling the small angle scattering of SBA-15 is well-established and previous investigators have used models of varying degrees of complexity [25,42–44]. The hydrostatic SBA-15 SAXS data was fit using a simple model focused on capturing the behavior of the ordered peaks. Modelling used four separate contributions: diffraction peaks from the ordered mesopore lattice (mesolattice), a Guinier-Porod contribution, a low-*q* power law, and an instrument background:

$$I(q) = I_{ordered}(q) + I_{Guinier-Porod}(q) + I_{Power\,Law}(q) + I_{background} \qquad (1)$$

$I_{ordered}(q)$ comes from the mesolattice structure of SBA-15, which consists of long, cylindrical pores arranged in a 2D hexagonal mesolattice [21]. This contribution is modeled by five pseudo-Voigt peaks (area-normalized so that the intensity equals the area under the peak) with locations in *q* determined by the five lowest order hk reflections of a 2D hexagonal mesolattice (*P*6*mm*) [43]. $I_{Guinier-Porod}(q)$ uses Hammouda's model to represent diffuse scattering from the nanometer-scale pore walls [45]. We used a cylindrical form factor for the Guinier-Porod contribution and fixed the Porod exponent at -4. The low-*q* scattering was modeled using a power law, $I_{Power\,Law}(q) = C * q^{\alpha}$, where C is a constant and α, the scattering exponent, is fixed to -4. The low-*q* scattering likely arises from the surfaces of the largest scattering structures in the sample, which in SBA-15 is the micron-sized particles [25,42]. The instrument background was modeled as constant.

SI Section 2.1 shows a representative SBA-15 SAXS fit broken out into its components.

3.2 WAXS Modelling

WAXS fitting used a simple model focused on capturing the behavior of the FSDP and gold diffraction peak. The model used five separate contributions as shown in Eq. (2): a power law scattering contribution for the low-*q* scattering, a flat instrument background, a Gaussian peak representing the gold diffraction (111) reflection, and two Gaussian peaks making up the FSDP (representing the high-*q* and low-*q* components).

$$I(q) = I_{Power\,Law}(q) + I_{Gold}(q) + I_{FSDP,\,High-q}(q) + I_{FSDP,\,Low-q}(q) + I_{background} \qquad (2)$$

The power law low-*q* scattering behavior is also found in previous WAXS measurements of mesoporous silica [15]. This contribution likely arises from density fluctuations in the *a*SiO_2 walls. The diffraction peak is from gold particles added to the SBA-15 powder as a hydrostatic pressure probe (see next section). The FSDP is modelled using two peaks based on the primary features of the data. Only the low-*q* peak (the highest-intensity,

principal component) was used to monitor FSDP position, FWHM, and intensity (as is common to most *a*SiO_2 studies).

SI Section 2.2 shows a representative SBA-15 WAXS fit broken out into its components.

3.3 Hydrostatic Pressure

The hydrostatic pressure exerted on the *a*SiO_2 walls of SBA-15 was calculated from the gold unit cell volume, determined from the (111) diffraction reflection, using a third-order Birch-Murnaghan EOS [46,47] and the parameters given in Anderson et al [48]. The systematic error in pressure was estimated at ~0.1 GPa, peak fitting errors were comparatively negligible (~2 orders of magnitude smaller).

This calculation assumes that the pressure exerted by the PTM on the *a*SiO_2 pore walls is hydrostatic and equivalent to that on the gold particles. For this to be true, the PTM must fully penetrate the pores. A previous study, using contrast-matched small angle neutron scattering (CM-SANS), showed that isooctane almost entirely penetrates the pore volume in SBA-15 (~10^{-4} cm^3/g void volume remaining) [25]. Smaller molecules like n-decane (cross-sectional diameter ~4.9 Å [49]) completely fill all pores leaving no measurable void volume. n-decane is larger than methanol or ethanol (cross sectional diameters of ~3.8 Å and ~4.4 Å respectively), indicating our PTM should fully occupy the pore space in SBA-15.

During SBA-15 hydrostatic compression, we assume that a fully pore-penetrating hydrostatic PTM (1) remains hydrostatic and pressure-equilibrated to the external PTM when inside nanoscale-sized pores, (2) stabilizes the pores against collapse so that porosity does not significantly affect SBA-15's compressibility, and (3) does not itself have a significant effect on SBA-15's compressibility. This implies that the DAC compresses only the SBA-15 skeletal structure, so the measured compressibility of the mesolattice reflects that of *a*SiO_2 alone without PTM or porosity contributions. See Appendix A for a detailed defense of these assumptions.

3.4 Volumetric Compression and Densification

Volumetric compression of the *a*SiO_2 walls is calculated $V_{norm}=a^3/a_0^3$, where $V_{norm}=V/V_0$ is the volume normalized to its ambient pressure value, a is the compressed 2D hexagonal mesolattice parameter, and a_0 is the ambient mesolattice parameter (see SI Section 2.3 for derivation). However, mesolattice diffraction does not directly measure *a*SiO_2 wall width and the 2D mesolattice lacks c-direction data for volume calculations (Fig. 1b). We estimate *a*SiO_2 volumetric compression by assuming: (1) the contraction, i.e. linear strain, of the *a*SiO_2 wall thickness is the same as that of

the mesolattice parameter, and (2) linear strain is the same in all crystallographic directions (including the *c*-direction) at any given hydrostatic pressure.

Both assumptions hold if SBA-15 undergoes linear isotropic compression, where a hydrostatic PTM distributes pressure equally in all directions resulting in uniform strains in all directions for isotropic materials. Assuming linear isotropic compression is common for hydrostatic compression of bulk a-SiO_2 [50]. Given that all bulk polyamorphs of a-SiO_2 are isotropic, it is likely that SBA-15 – which is microstructurally similar to fused silica – is also isotropic. While isotropic compression is straightforward for the *a*- and *b*-directions, it is more complex for the *c*-direction due to mesopore vertical alignment (Fig. 1). Nonetheless, we approximate linear isotropic compression for the *c*-direction because (a) the bulk material's isotropy is more relevant than particle shape anisotropy during hydrostatic compression, and (b) the hydrostatic environment for SBA-15 should be uniform due to long equilibration times and complete PTM pore penetration.

3.5 EOS modelling

SBA-15 densification during hydrostatic compression was modelled using an EOS transition between a low- and a high-pressure densification regime. Both regimes are modeled using third-order Birch-Murnaghan EOSs [46,47,51]. A third-order Birch-Murnaghan EOS describes the change in V_{norm} under compressive pressures using two parameters K_0 and K'_0, the bulk modulus at ambient pressure and the first derivative of the bulk modulus at ambient pressure respectively. At a transition density, defined as the coordinate where the low- and high-pressure EOSs intersect, the model instantaneously transitions from following the low-pressure EOS to following the high-pressure EOS. This model was chosen for its simplicity and does not imply the order of the transition mechanism.

The simple EOS transition model has fitting parameters $\rho_{0,Low\text{-}P}$, $K_{0,Low\text{-}P}$ and $K'_{0,Low\text{-}P}$ for describing the low-pressure regime, and $\rho_{0,High\text{-}P}$, $K_{0,High\text{-}P}$ and $K'_{0,High\text{-}P}$ for describing the high-pressure regime. Errors for fitted parameters were defined the same as for SAXS and WAXS. Fits were weighted using $\sigma_{V_{norm}}$, propagated from the hexagonal mesolattice parameter fitting errors.

Models with transitions between multiple EOSs are commonly used to describe phase or microstructural transitions in oxide glasses [16,52]. A detailed description of the equations and calculations for the simple EOS transition model is given in SI Section 2.4.

4.0 Results for hydrostatic compression

4.1 Small Angle X-ray Scattering

[Insert Figure 2 here]

Figure 2 shows SAXS data and corresponding fits for the hydrostatic compression of SBA-15 [53]. At ambient pressure, the ordered SBA-15 mesopores give rise to a series of diffraction peaks including higher order reflections. This signifies a high degree of order between the mesopores. The SAXS data at 0 GPa match a *P*6*mm* space group (2D hexagonal) with mesolattice parameter a_0 = 118.9 Å, in agreement with previous literature [21,24,25,42]. Under applied hydrostatic pressure, the peaks shift to higher *q*, decrease in intensity, and become broader, indicating a shrinking mesolattice and increasing mesolattice disorder (Fig. 3). The mesolattice peaks match a *P*6*mm* space group across the full pressure range.

Figure 3 displays the integrated peak intensity and FWHM of the low-*q* peak as a function of hydrostatic pressure. At ~3 – 4 GPa there is an inflection in both the peak intensity and FWHM. Decreasing peak intensity and increasing FWHM signify more disorder.

The Guinier-Porod scattering contribution could be fit using a range of different inputs (i.e. no unique solution), thus necessitating simplifying approximations. The form factor was estimated as cylinders (dimensionality=2) based on goodness of fit and rough agreement with the shape of the *a*SiO_2 skeletal structure. The Porod exponent was estimated as -4 corresponding to smooth surfaces. This fit $R_{cylinder} \approx 9$ Å, in general agreement with scattering structure sizes from previous studies [25,42]. Uncertainty in $R_{cylinder}$ precluded determination of its pressure sensitivity. Previous studies used spherical form factors, so a different source of density fluctuations may be dominating the diffuse scattering in our sample. The fitted scattering structures are too large to arise from microporosity but similar in scale to the SBA-15 *a*SiO_2 pore walls, suggesting that they themselves are the source of the diffuse scattering.

The low-*q* power law region, which corresponds to the micron-sized SBA-15 particles, fit well across the full range of pressures with the estimated power law exponent $\alpha = -4$. This corresponds to smooth particle surfaces and agrees with previous studies [25,42].

[Insert Figure 3 here]

4.2 Wide Angle X-ray Scattering

[Insert Figure 4 here]

Figure 4 shows WAXS data and corresponding fits for SBA-15 under hydrostatic compression [53]. The main WAXS feature for SBA-15 is the FSDP. At ambient pressure, SBA-15's FSDP is at q = 1.69 ± 0.01 Å^{-1}. This is much higher than for fused or vitreous silica (q = 1.52 Å^{-1}) [16,38,54,55], consistent with previous studies showing that SBA-15's FSDP is higher in q, significantly broader, and lower-intensity [15,22]. Under increasing hydrostatic pressure, the FSDP position shifts to higher q values and transitions to a less pressure-sensitive regime (Fig. 5). This is consistent with the real-space structures in the IRO that give rise to the FSDP getting smaller and less compressible with increasing pressure. The behavior of the minor component of the FSDP is described in SI Section 6. Throughout the entire compression measurement there are no signs of any crystalline SiO_2 contributions or pressure-induced crystallization, which would have caused diffraction signals in the measured q range. The vertical feature near $q \approx 2.6$ Å^{-1} is the gold (111) diffraction reflection, used to measure pressure inside the chamber.

The relationship between SBA-15's ambient pressure FSDP position and its skeletal density (ρ = 2.42 ± 0.02 g/cm^3) aligns closely with the trends observed by Tan and Arndt [56] and Salmon et al [2] for bulk *a*SiO_2 polymorphs (see SI Section 4). These previous studies demonstrate a linear relationship between the ambient FSDP position and ambient density. Therefore, the high q FSDP position of SBA-15 at ambient pressure is likely due to its higher skeletal density (not its ring size distribution, as has been previously suggested [4,15]). This suggests that the FSDP of SBA-15 shares a common origin with that of fused silica and that the materials have closely related microstructures.

Figure 5 shows the integrated peak intensity and FWHM of the low-q FSDP component as a function of hydrostatic pressure. The intensity initially increases, and then starts to decrease after an inflection point at ~3 GPa. The brief period (< ~3 GPa) where the intensity of the low-q component is increasing signals an increase in the number of FSDP scattering structures, which in turn suggests an increase in the amount of order in the *a*SiO_2 IRO. The inflection point occurs at approximately the same pressure as the changes in the SAXS peaks shown in Figure 3. The FWHM increases (largely monotonically) over the measured pressure range, indicating increasing disorder.

[Insert Figure 5 here]

5.0 Discussion

5.1 Evidence for direct, hydrostatic compression of the *a*SiO_2 skeletal structure

[Insert Figure 6 here]

During hydrostatic compression of SBA-15, SAXS measurements of mesolattice contraction likely reflect the densification of the *a*SiO_2 skeletal structure (i.e. walls) without contributions from porosity or the pressure transmitting medium (PTM). As evidence, we first compare the hydrostatic compression of SBA-15 against the hydrostatic compression of fused silica.

Figure 6 compares the densification of SBA-15 under hydrostatic compression against the hydrostatic densification of fused silica and the uniaxial (non-hydrostatic) densification of SBA-15. Methods for fitting the uniaxial SBA-15 data are detailed in SI Section 5, along with representative uniaxial WAXS and SAXS fits and a waterfall plot of the fitted uniaxial SAXS data.

Figure 6 shows that the compressibility of hydrostatic SBA-15 closely matches that of fused silica. A linear fit of the three lowest-pressure points gives an initial bulk modulus for SBA-15 of ~35 GPa, aligning well with that of fused silica (~37 GPa) [50]. Because nanoscale materials in hydrostatic compression typically exhibit moduli within ~30% of their bulk equivalents [57–60], this suggests the DAC directly compresses the aSiO_2 walls and that alternative densification contributions are not significant.

Comparing the hydrostatic versus uniaxial (non-hydrostatic) compression of SBA-15 evidences the stabilization of pores against collapse by a penetrating PTM. The ambient-pressure mesolattice parameter of the uniaxial measurement (which was measured in air), a_0 = 119.1 Å, matches that of the hydrostatic case. This suggests there was no crushing of the SBA-15 pores during the initial DAC setup or mesolattice strain caused by the pore-penetrating PTM. Figure 6 shows that uniaxially compressed SBA-15 is more compressible, with an initial pseudo bulk modulus of ~2.2 ± 0.2 GPa. This is more than an order of magnitude lower than hydrostatic SBA-15 and agrees with the expected reduced modulus, ~1 GPa, from un-stabilized porosity (via the Mackenzie equation, see SI Section 5.5) [61]. The uniaxial compression experiment illustrates how our hydrostatic sample compressibility would change if the pores were not stabilized.

During uniaxial compression, both the SAXS peaks and the WAXS gold diffraction peak become asymmetric as soon as significant non-hydrostatic force was applied (SI Figure 12). As the pores collapsed, uniaxial SAXS peaks lost their intensity, widened, and reduced to only two discernable peaks. During hydrostatic compression these problems are absent, suggesting hydrostatic conditions were maintained.

5.2 First Sharp Diffraction Peak

[Insert Figure 7 here]

Figure 7 shows the FSDP position as a function of hydrostatic pressure for SBA-15 and several other *a*SiO_2 polyamorphs. The behavior of the fused silica FSDP position with pressure is used as the main benchmark for our SBA-15 results. At low pressures, the fused silica FSDP position has a high rate of change with pressure (dq_{FSDP}/dP) and an approximately linear relationship to pressure. This is followed by a transition at ~12 – 15 GPa to a high-pressure regime which is also approximately linear, has a smaller dq_{FSDP}/dP, and extends to ~40 GPa [10,38]. The low-pressure FSDP regime with large dq_{FSDP}/dP coincides with a high rate of rearrangement for the intertetrahedral bonding (and thus changes to the IRO) and minor changes to Si-O intratetrahedral bonds [38,62]. The high-pressure FSDP regime with smaller dq_{FSDP}/dP coincides with less rearrangement of the intertetrahedral bonding indicating stiffer IRO structures and major changes to the intratetrahedral bonds [38] (because > ~16 GPa the main compression mechanism is the Si coordination change [10,38,63]). SBA-15 has an FSDP transition from high dq_{FSDP}/dP to low dq_{FSDP}/dP like fused silica (from now on just referred to as an FSDP transition), but at a much lower pressure of ~0.5 – 3 GPa (Fig. 5). Importantly, for both fused silica and SBA-15 the FSDP transition happens at approximately the same pressure as the LDA-to-HDA EOS transition (described in the next section), suggesting a shared mechanism.

Other polyamorphs of *a*SiO_2 in Figure 7, densified fused silica [16] and fused silica with dissolved helium [54], have only low dq_{FSDP}/dP regimes (and no FSDP transitions) likely due to their significantly reduced interstitial void space, which makes structures within the IRO less compressible.

Another *a*SiO_2 polymorph in Figure 7, fumed silica, is notable for having a larger dq_{FSDP}/dP than fused silica [13]. This highly pressure-sensitive fumed silica regime continues until ~6 GPa, where it likely starts having an FSDP transition. Similar to the fused silica low-pressure, large dq_{FSDP}/dP regime, this fumed silica regime was shown to be concurrent with a high rate of decrease in Si-O-Si angles (i.e. rearrangement of IRO structures) and minimal change to Si-O bond lengths and angles [13].

Like for fused silica, SBA-15 has an FSDP transition from a low-pressure regime with large dq_{FSDP}/dP to a high-pressure regime with smaller dq_{FSDP}/dP (Fig. 5). However, Figure 7 shows that SBA-15's dq_{FSDP}/dP is exceptionally large compared to that of fused silica and all other *a*SiO_2 polymorphs shown in Fig. 7. At low pressures (i.e., less than ~0.75 GPa) SBA-15's dq_{FSDP}/dP, ~0.24 $Å^{-1}·GPa^{-1}$, is seven times larger than that of fused silica's low-pressure regime, ~0.03 $Å^{-1}·GPa^{-1}$, and three times that of fumed silica, ~0.07 $Å^{-1}·GPa^{-1}$. In this highly pressure-dependent FSDP regime, it is likely that the IRO is

rapidly rearranging while the short-range order remains largely unchanged, like for fused silica and fumed silica. After its FSDP transition, SBA-15's dq_{FSDP}/dP decreases by almost an order of magnitude to ~0.03 $Å^{-1}·GPa^{-1}$ (Fig. 5) which is close to the dq_{FSDP}/dP of the fused silica low-pressure regime. This is larger than the dq_{FSDP}/dP of either the fused silica high-pressure regime or densified fused silica (both ~0.01 $Å^{-1}·GPa^{-1}$) and much larger than the dq_{FSDP}/dP of fused silica with dissolved helium (~0.004 $Å^{-1}·GPa^{-1}$). It is likely that the IRO is rearranging more slowly in the SBA-15 high-pressure, small dq_{FSDP}/dP regime and that the intertetrahedral network has become less compressible, like for after the FSDP transition in fused silica.

While both SBA-15 and fumed silica have FSDP positions that start out with larger dq_{FSDP}/dP than fused silica, there are still significant differences in their FSDP behavior. The ambient pressure FSDP position for SBA-15 is higher than for fumed silica nanoparticles, so the real-space structures in the IRO which give rise to the FSDP are smaller in SBA-15 than in fumed silica. The fumed silica FSDP position versus pressure slope is linear, like fused silica, up to ~6 GPa. The SBA-15 FSDP position pressure-dependence is not linear throughout most of the compression measurement.

5.3 Volumetric Compression and Equation of State

[Insert Figure 8 here]

The hydrostatic, volumetric compression of SBA-15 is compared to different *a*SiO_2 polyamorphs in Figure 8. The behavior of fused silica is used to benchmark our SBA-15 results. At moderate pressures up to ~15 GPa, where fused silica is entirely tetrahedrally coordinated [10,17,38,63], the compression of fused silica can be mostly described using two EOSs: an LDA-type EOS and an HDA-type EOS. The LDA-type EOS corresponds to fused silica at pressures below ~7 GPa [50,64], and the HDA-type EOS corresponds to densified fused silica [16]. During a continuous compression experiment (i.e. when the pressure is monotonically increased up to the maximum pressure) up to ~15 GPa, fused silica undergoes a transition at ~11-15 GPa from an LDA EOS to an HDA EOS [16,64].

Fused silica exhibits an LDA-type EOS within the compression range shown in Figure 8, for which the dominant densification mechanism is the rearrangement of the IRO structures (bending and rotation of the bridging oxygen bonds) resulting in the reduction of interstitial voids [16,54]. Meanwhile the short range order, i.e. the SiO_4 tetrahedra, is minimally affected [10,38]. During compression of fused silica in the HDA regime, the intertetrahedral bonds are already strained [3] and the interstitial void space greatly reduced [16], making the IRO structures and intertetrahedral network less compressible.

Densified fused silica [16] and fused silica with dissolved helium [54] do not have strongly pressure-dependent FSDP regimes or LDA-type EOS regimes (Fig. 8). These materials don't have an LDA-type EOS regime because they already have significantly reduced interstitial void space and, in the case of densified fused silica, strained intertetrahedral bonds.

Figure 8 shows the fit of the EOS transition model to the densification of SBA-15. The model accurately replicates the behavior of SBA-15. See Supporting Information for a detailed description of the fitting process (SI Sections 3.1 and 3.2) and comparisons of several fitting iterations with fitting errors (SI Section 3.3).

To constrain the EOS transition model fit shown in Figure 8, K'_0 was fixed at 4 for both the low- and high-pressure EOSs and ρ_0 was fixed to the measured value of 2.42 g/cm^3 for the low-pressure EOS (see SI section 1.3 for pycnometry measurement). Note that fixing $K'_0 = 4$ is equivalent to a second-order Birch-Murnaghan EOS. Fitting obtained bulk moduli values of $K_0 = 35.1 \pm 0.6$ GPa for the low-pressure EOS, and $K_0 = 62.5 \pm 2.4$ GPa and $\rho_0 = 2.459 \pm 0.004$ g/cm^3 for the high-pressure EOS, corresponding to a transition point at $P_{Transition} = 1.5 \pm 0.4$ GPa and $\rho_{Transition} = 2.516 \pm 0.021$ g/cm^3. Note that the density error from model fits reflects the error for percent densification, not for the actual density values for ρ_0 and $\rho_{Transition}$.

Good fits with the EOS transition model could also be attained by fixing the bulk moduli of the low- and high-pressure EOS regimes to literature values of LDA fused silica [65] and densified fused silica [16] (SI Section 3.3). In addition, we investigated a modified EOS transition model where the instantaneous EOS transition is replaced with a transition zone in which the bulk modulus gradually switches between the two regimes (see SI Section 2.5 for detailed description). The modified EOS transition model fit the data with very low error and suggests SBA-15 could have a graded EOS transition spanning a pressure range of ~0.4 – 2.6 GPa (SI Section 3.3). This pressure range agrees with the error range of the transition pressure from the simple EOS- transition model.

Thus, all the variations of the EOS transition model fit the SBA-15 compression data with similar physically reasonable values. The EOS transition model fits all indicate that (1) the SBA-15 compression data is consistent with a transition between two separate EOSs, (2) the bulk modulus for the low-pressure EOS is close to that of LDA fused silica, (3) the bulk modulus for the high-pressure EOS is close to that of HDA fused silica, (4) the transition between the low- and high-pressure EOSs takes place at ~1 – 2 GPa, and (5) the ambient pressure density of the high-pressure EOS is approximately 2.46 ± 0.01 g/cm^3.

Several alternative types of EOS models were also tested to fit SBA-15 densification: a third-order Birch-Murnaghan EOS [46,47], a fourth-order Birch-Murnaghan EOS [46,47], and a model approximating the elastic anomaly in fused silica (SI Section 2.6). However, none of the alternative models could fit the SBA-15 densification data when constrained to physically realistic values, showing that they do not reflect the underlying compression mechanisms (Appendix B).

The SBA-15 low-pressure EOS likely corresponds to an LDA regime and the high-pressure EOS to an HDA regime, with the transition indicating an amorphous-amorphous microstructural transition. The bulk moduli for the SBA-15 low- and high-pressure EOSs are very close to the LDA and HDA bulk moduli for fused silica, a closely related *a*SiO_2 polyamorph. With regards to other possible explanations for a discontinuous EOS: There are no crystalline diffraction peaks, indicating no pressure-induced crystallization. There are no indications of pore collapse during hydrostatic compression (Section 5.1 and Appendix A). The poor fit of the model approximating the elastic anomaly to the data (Appendix B) and the higher proportion of small rings in SBA-15 (which reduces the proportion of six-membered rings supposedly responsible for the elastic anomaly [66]) suggest it is unlikely that the transition stems from a mechanism similar to the fused silica elastic anomaly. There is no WAXS peak appearing at ~3 $Å^{-1}$ during compression which would indicate sixfold coordinated Si [10], nor does the oxygen packing factor get large enough to suggest an increase in Si coordination number would be favorable [17]. There is no significant adsorption strain caused by the PTM (Section 5.1). Lastly, there are no compressibility changes caused by penetration of the PTM into bulk *a*SiO_2 interstitial voids. Methanol and ethanol have been shown to be insoluble into bulk *a*SiO_2 up to 10 GPa [54], and even a smaller molecule like argon cannot penetrate into bulk *a*SiO_2 or silica zeolites up to at least 8 GPa [60,67]. Thus, it is assumed for the remainder of the paper that the SBA-15 EOS transition is an LDA-to-HDA transition.

The LDA-to-HDA EOS transition for SBA-15 takes place at much lower pressure than in fused silica (~1.5 versus ~13 GPa). The only similar behavior previously observed was in fumed silica nanoparticles, where the onset of permanent densification takes place at a much lower pressure than for fused silica [68]. Permanent densification is likely related to the fused silica LDA-to-HDA transition [16]. The SBA-15 LDA-to-HDA EOS transition also occurs at a smaller densification ratio than for fused silica (~3.5% versus ~41%) and at a lower density (~2.51 versus ~3.12 g/cm^3) [16].

5.4 Relationship between FSDP and EOS

For both SBA-15 and fused silica, the pressure ranges for the EOS transition and the FSDP transition coincide. This suggests that the transition mechanisms are linked. Previous studies on oxide glasses, like GeO_2 and aluminosilicates, also found FSDP transitions co-located with EOS transitions and asserted a similar connection [52,69]. Notably, the current study demonstrates that altering the structure of a glass system (e.g., using a different *a*SiO_2 polyamorph) causes the pressure of both the FSDP and EOS transitions to shift in tandem.

Assuming the EOS transition pressures of SBA-15 (~1 – 2 GPa) and fused silica (~12 – 14 GPa) indicate their LDA-to-HDA transitions, the transitions occur at similar FSDP position ranges ($q \approx 1.90 – 1.98$ Å^{-1} and $q \approx 1.92 – 1.98$ Å^{-1} respectively) [16]. This suggests that during cold compression the EOS transition may occur at a critical FSDP position for all *a*SiO_2 polyamorphs, possibly because the IRO structures and FSDP are closely related among all aSiO_2 polymorphs.

The correlation in transition pressures for FSDP and bulk *a*SiO_2 compression are unsurprising. The rearrangement of the intertetrahedral network is the dominant compression mechanism for LDA fused silica, and a significant mechanism for HDA fused silica [16]. The rearrangement of the intertetrahedral network is also the primary driver of change in the IRO. Because change in the FSDP signifies change happening in the IRO, one would expect that *a*SiO_2 compression is closely correlated with the FSDP behavior.

Despite this connection, comparison of Figures 7 and 8 reveals that the rate of change of the FSDP position with pressure, dq_{FSDP}/dP, is not indicative of the *a*SiO_2 bulk modulus. Figure 7 shows that dq_{FSDP}/dP is much larger for SBA-15 than for fused silica. If we assume that the FSDP in both materials manifests from the same real-space structures in the IRO - as evidenced by both materials following the same ambient pressure FSDP position versus density trend - then the difference in dq_{FSDP}/dP must be due to the FSDP structures rearranging at a higher rate in SBA-15 than in fused silica. Figure 8 shows that SBA-15 and fused silica have approximately the same bulk modulus, especially for the LDA EOS. Thus, the FSDP structures rearrange at a higher rate in SBA-15 than in fused silica, but both materials densify at the same rate. This suggests that, during cold compression, the rearrangement of the FSDP structures does not significantly affect the density of *a*SiO_2 and thus there is no direct correlation between the FSDP position and the bulk modulus in *a*SiO_2. This finding is consistent with recent research indicating that the collapse of intertetrahedral rings significantly contributes to *a*SiO_2 densification, and the FSDP is uncorrelated to the size or collapse of these rings [2].

This finding has two important implications. First, if intertetrahedral ring collapse is indeed a major contributor to densification, then the discrepancy between the pressure dependence of the FSDP position and the bulk modulus is further evidence that the FSDP does not originate from these rings. This inference challenges ring size-based models for the origin of the FSDP [4,7] and supports alternative models based on IRO structures with minimal densification impact. Second, the densification of *a*SiO_2 cannot be monitored using the FSDP position. Although d_{FSDP} (FSDP correlation length $d = 2\pi / q_{FSDP}$) decreases much faster than bulk *a*SiO_2 densifies which indicates the FSDP position cannot directly measure densification [56], it has remained a common assumption that dq_{FSDP}/dP qualitatively reflects the glass densification rate. This is because both FSDP positional changes and densification of LDA *a*SiO_2 are strongly correlated with the rearrangement of the IRO. This assumption is inconsistent with the current results.

The inflection region for the intensity and FWHM of the SBA-15 SAXS peaks and FSDP (~3 – 4 GPa, Fig. 3 and 5) may signify a change in the compression mechanism. Because the inflections occur at higher pressures than the FSDP or EOS transitions, the change in compression mechanism would be unrelated to those transitions. Regardless, inflection regions occurring at the same pressure for both SAXS and WAXS peaks is further evidence of a correlation between the FSDP and bulk material compression.

5.5 Comparing the Equation of State and Density of SBA-15 with Fused Silica

Previous literature has found that the ambient compressibility of *a*SiO_2 is closely tied to its ambient density [70], so that fused silica and its partially densified counterparts all follow the same density versus bulk modulus trend. In the current work, SBA-15 is shown to significantly deviate from this trend. The SBA-15 LDA regime has an ambient density of 2.42 g/cm^3, which would correspond to a bulk modulus of $K_0 \approx 42.5$ GPa according to previous literature [70]. However, this modulus is inconsistent with our SBA-15 LDA compression data, which has approximately the same bulk modulus as LDA fused silica (2.20 g/cm^3). Similarly, the SBA-15 HDA EOS has an effective ambient density of ~2.46 g/cm^3 and a bulk modulus close to a highly densified fused silica (2.67 g/cm^3) [16], which is inconsistent with the expected bulk modulus of $K \approx 46.4$ GPa according to the previous literature [70]. Thus, it is likely that the compressibilities of different types of *a*SiO_2 materials have different correlations with their ambient densities.

This is a somewhat surprising result in that SBA-15 and fused silica follow the same ambient-pressure FSDP vs density trend (SI Section 4) and have closely related microstructures. While it is possible that the differences in compressibility vs. density between SBA-15 and fused silica arise from minor changes in the ring size distribution

or other IRO features, the difference is most likely due to the nanoscale nature of SBA-15. Previously, it was found from FTIR that the Si-O-Si bonds in nanoscale fumed silica are more flexible than compared to fused silica, have a slightly shifted stretching band, and their bond angles change more under applied pressure [37,71]. This suggests that, in general, nanoscale *a*SiO_2 particles may have a more flexible intertetrahedral network with different Si-O-Si bond responses to pressure and density.

5.6 First Sharp Diffraction Peak pressure sensitivity and LDA-to-HDA transition at low pressure

It is challenging to determine the underlying cause of the extreme FSDP pressure-sensitivity (i.e. very high dq_{FSDP}/dP) and the shift of the LDA-to-HDA EOS transition to lower pressures for SBA-15 compared to fused silica. Uchino et al attributed the lower LDA-to-HDA transition pressure of fumed silica to a smaller bulk modulus by using dq_{FSDP}/dP as a proxy for the bulk modulus [13]. However, we showed that dq_{FSDP}/dP is not indicative of the bulk modulus, and that nanoscale LDA *a*SiO_2 has a similar bulk modulus to fused silica. The FSDP pressure-sensitivity and EOS transition shift are also not likely due to differences in chemistry or the IRO between SBA-15 and fused silica. Uchino et al found that high-temperature calcined fumed silica nanoparticles - which has an IRO similar to fused silica and should have much fewer hydroxyl impurities [37] - also had higher FSDP pressure-sensitivity than fused silica [13]. In addition, the levels of hydroxyl impurities in SBA-15 are relatively small and almost totally segregated to the external and pore surfaces (see SI Section 1.5).

The FSDP pressure-sensitivity is most likely due to the few-nanometer thin walls of SBA-15. As discussed in the previous section, the flexibility of Si-O-Si bonds in *a*SiO_2 is likely enhanced in nanoscale particles. The increased flexibility of these bonds could allow the intertetrahedral network to rearrange more under the same amount of pressure, which would also make the FSDP more sensitive to pressure. This hypothesis is evidenced by comparing the compressibility of bulk *a*SiO_2 against the pseudo-compressibility of the FSDP for different *a*SiO_2 polyamorphs (Appendix C). Polyamorphs which likely have stiffer intertetrahedral networks have smaller compressibility differences between the bulk and the FSDP.

The lower-pressure EOS transition is also most likely due to the nanoscale nature of SBA-15. Studies on crystalline nanoparticles commonly find that nanoparticle size changes the pressure at which a phase transition occurs [59,72–74]. The lower EOS transition pressure may be explained by the interfacial free energy penalty between an HDA nucleus and the LDA volumetric phase (analogous to crystalline nanoparticles [72]). The magnitude of this energy penalty is proportional to the interfacial area

between the original phase and the nucleated phase. In bulk materials the interfacial area is assumed to be the entire surface area of the spherical nucleus. However, in SBA-15 the thin walls (~2 – 3 nm) result in part of the nucleus bordering the pore surface and the reduced interfacial area between HDA and LDA phases decreases the free energy penalty. Additionally, enhanced Si-O-Si bond flexibility could reduce the misfit strain energy and the interfacial energy per unit area between the HDA and LDA phases [72]. Overall, the decreased interfacial energy lowers the nucleation energy barrier and facilitates a microstructural transition at lower pressure. The HDA microstructural transition would lead to a stiffer network and thus decrease the pressure sensitivity of the FSDP.

Further research on nanoscale *a*SiO_2 polyamorphs is necessary to test these hypotheses for the increased FSDP pressure-sensitivity and the lower LDA-to-HDA transition pressure in SBA-15 and fumed silica.

6.0 Conclusion

The densification and FSDP of SBA-15 under GPa pressures was measured by SAXS and WAXS in-situ in a diamond anvil cell. The EOS of SBA-15 has an LDA-to-HDA transition like fused silica, but at much lower pressures. The pressure dependence of the FSDP position for SBA-15 was higher than for fused silica and similar to fumed silica nanoparticles.

This study indicates that (1) the FSDP transition in *a*SiO_2 materials signals the onset of the LDA-to-HDA EOS transition, (2) there is no direct relationship between the rate of change of the FSDP position with pressure and the *a*SiO_2 bulk modulus, (3) the compressibility of *a*SiO_2 materials is not necessarily a function of their ambient density, and (4) at ambient pressure, the skeletal density and FSDP position of SBA-15 map onto the same linear relationship observed for other *a*SiO_2 polyamorphs. Additionally, we hypothesize a critical range for d_{FSDP} common to all *a*SiO_2 polyamorphs at which the EOS LDA-to-HDA transition occurs.

Glossary

aSiO_2: amorphous silica dioxide.

SBA-15: a periodic mesoporous material where the bulk/wall material is *a*SiO_2.

TEOS: tetraethyl orthosilicate, an organic silicate that is used as a precursor for silicon dioxide.

IRO: Intermediate Range Order, encompassing the ordering arising from intertetrahedral bonding between the SiO_4 units on length scales between ~5 – 50 Å.

FSDP: First Sharp Diffraction Peak, a common and important feature in the WAXS/XRD spectrum of oxide glasses (as well as other amorphous materials) which arises due to intermediate range ordering.

SAXS: Small Angle X-ray Scattering, a scattering technique used for detecting features in the size range of nanometers to tens of nanometers, typically covering a q range between ~0.01 – 0.5 $Å^{-1}$.

WAXS: Wide-Angle X-ray Scattering (WAXS), a scattering technique used to probe ordering on the atomic length scale. Very similar to X-ray Diffraction

EOS: Equation of State, describes the relationship between pressure and volume.

LDA/HDA: Low Density Amorphous and High Density Amorphous, commonly used to denote a microstructural change in an amorphous material.

DAC: Diamond Anvil Cell, a scientific apparatus used to create extreme hydrostatic pressures >1 GPa.

PTM: Pressure Transmitting Medium, the fluid that surrounds the SBA-15 sample and fills the DAC sample chamber, and which can transmit the pressure from the DAC to the sample hydrostatically.

Acknowledgements

The authors would like to thank Professor Sabyasachi Sen for helpful discussions and introductions.

Funding

This work was supported by the UC Lab Fees Fellowship from University of California Research Initiatives (Contract No. LGF-20-652903); and by the U.S. Department of Energy through the Los Alamos National Laboratory. Los Alamos National Laboratory is operated by Triad National Security, LLC, for the National Nuclear Security Administration of U.S. Department of Energy (Contract No. 89233218CNA000001). Portions of this work were performed at HPCAT (Sector 16), Advanced Photon Source (APS), Argonne National Laboratory. HPCAT operations are supported by DOE-NNSA's Office of Experimental Sciences. The Advanced Photon Source is a U.S. Department of

Energy (DOE) Office of Science User Facility operated for the DOE Office of Science by Argonne National Laboratory under Contract No. DE-AC02-06CH11357.

Declaration of Interests

The authors report there are no competing interests to declare.

Authorship Contribution Statement – CrediT

Michael R. Bull: Conceptualization, Formal Analysis, Investigation, Visualization, Writing – original draft, review and editing. Rachel C. Huber: Investigation. Ping Yu: Investigation. Tanner J Finney: Investigation, Writing – review and editing. Noah Felvey: Investigation. Paul Chow: Investigation. Yuming Xiao: Investigation. Tonya L. Kuhl: Writing – original draft, review and editing. Erik B. Watkins: Conceptualization, Formal Analysis, Investigation, Visualization, Writing – original draft, review and editing.

Data Availability Statement

The data that support the findings of this study ("In-situ SAXS and XRD of SBA-15 in a Diamond Anvil Cell during high-pressure densification") are openly available in Mendeley Data at http://doi.org/10.17632/4sncvxbn6x.1, reference number [53].

Declaration of generative AI and AI-assisted technologies in the writing process

During the preparation of this work the authors used ChatGPT in order to improve the manuscript's readability and conciseness. After using this tool/service, the authors reviewed and edited the content as needed and take full responsibility for the content of the published article.

Appendix A: Discussion of the Hydrostatic Pressure and Stabilizing Effects inside Mesopores Filled by a Pore-Penetrating PTM

During hydrostatic compression of SBA-15, we assume that the PTM (1) remains hydrostatic and pressure-equilibrated to the external PTM when inside nanoscale-sized pores, (2) stabilizes the pores against collapse, and (3) does not itself have any significant effect on the particles' compressibility.

Regarding assumption (1), problems that could prevent this include pore blockages or nanoscale confinement effects that would cause major deviations from bulk liquid behavior. First, pore blockages could trap the PTM in pockets or prevent the PTM from flowing freely into, out of, and through the pores and thus equilibrating with the surrounding environment. However, the SBA-15 porosity is highly interconnected, the mesopores are relatively large, and the PTM likely fully permeates all available pore space. This suggests any pore blockages or constrictions in SBA-15 are likely negligible.

Second, interactions between the PTM molecules and the pore walls can, especially for nanoscale pores, cause a difference of pressure inside vs outside of the pores ("capillary pressure"). Prior studies on small-molecule hydrocarbons in nanoscale pores show capillary pressures of ~0.1 MPa for molecules similar to our PTM [75]. This is several orders of magnitude below our systematic error for pressure. Lastly, deviations from hydrostatic behavior may arise if the pore size alters the PTM liquid "structure". But with ~95 Å mesopores and ~4 Å PTM molecules, adsorption layers should be minimal relative to pore volume [76]. Thus, the liquid "structure" inside the pores is likely almost the same as externally, especially considering the nearly ideal mixing behavior of methanol and ethanol.

Regarding assumption (2), if the porosity within the SBA-15 particles collapses then the compressibility of the mesolattice will greatly decrease [61]. However, if the PTM has fully penetrated the pores and is applying pressure hydrostatically, then the pores will not collapse and instead shrink at a rate proportional to the *a*SiO_2 walls (i.e. linear isotropic compression). Numerous high-pressure compression studies have confirmed this stabilization effect. For example, research on pressured-induced amorphization (PIA, a type of pore collapse occurring in nanoporous crystalline materials [77]) found for zeolites and MOFs that use of a pore-penetrating PTM eliminated (or greatly delayed) signs of PIA and pore collapse [60,78].

Regarding assumption (3), the only effect of the PTM on the compressibility of the SBA-15 mesolattice should be pore stabilization. The compressibility of the PTM itself should not affect our measurements. First, while trapped pockets of PTM could affect the mesolattice compressibility, as discussed above the PTM is unlikely to be trapped by pore blockages and can flow freely in and out of the SBA-15 structure. Second, pressure-induced pore emptying (squeeze-out) is ruled out because it causes a reduction in compressibility with pressure, opposite to our observations [79]. Third, external pressures can sometimes force significantly more liquid molecules into a pore space than at ambient pressure ("hyperfilling"), changing the porous material's compressibility [80]. However, this requires dominant pore/constriction dimensions similar in size to the PTM molecules and is typically accompanied by increases in the mesolattice size. Almost the entirety of SBA-15 porosity is at least several nanometers in diameter - the large majority more than 8 nanometers in diameter [25] - and the SBA-15 mesolattice does not expand upon uptake of or compression in the PTM.

Previous experiments have directly shown that pore-penetrating PTMs have no effect on the compressibility of nanoporous solids (other than stabilizing pores against collapse). The hydrostatic compressibility of brewsterite - a zeolite highly resistant to pore collapse and PIA – was shown to be the same when compressed in either a non-penetrating

PTM or a pore-penetrating PTM [81]. Its compression was completely unaffected by the PTM inside its nanoscale pores. Similarly, previous work has shown that compressing the same zeolites in different pore-penetrating PTMs results in no compressibility differences [60]. The PTMs had significantly different sizes and intermolecular interactions, such that one would expect a difference between the two if nanoscale confinement effects were affecting the compression experiments.

Appendix B: Fitting Alternative EOS Models to SBA-15 Densification

Three alternative EOS models were tested: a third-order Birch-Murnaghan EOS, a fourth-order Birch-Murnaghan EOS, and a model approximating the elastic anomaly in fused silica. The authors note that models involving more than one EOS transition were ruled out due to their unnecessary complexity. Also, trying other generalized EOSs than Birch-Murnaghan would not significantly change the fits because under 5 GPa all the generalized EOS formalisms are very similar [51].

Third-order Birch-Murnaghan EOS:

Initially, the SBA-15 compression data was fit using a single third-order Birch-Murnaghan EOS [46,47] with K_0 = 28.9 ± 1.3 GPa and K'_0 = 19.8 ± 2.3. However, such a large K'_0 is unphysical. A survey of previous literature studying single-phase EOSs for a range of materials like SBA-15 including crystalline oxides, metal and oxide glasses, nanoparticles, and mesostructured materials, showed that K'_0 is typically close to 4 and always less than 10 (SI Section 3.1). We found that the SBA-15 data simply cannot be fit with $K'_0 \leq 10$ GPa. The unusually large K'_0 in this fit is most likely due to a material transition happening during compression. For example, gold and PbS nanoparticles that fit to a similar K'_0 were shown to be undergoing a phase transition, meaning the large K'_0 was compensating for an improper single-phase EOS model fit to multi-phase data [82,83].

Fourth-Order Birch-Murnaghan EOS:

The fourth-order Birch-Murnaghan EOS [46,47] adds the second derivative of K with respect to pressure at 0 GPa (K''_0) as another fitting parameter. This gives it more freedom to fit unusual data. However, this model also cannot reproduce the SBA-15 data when K'_0 and K''_0 are constrained to physically reasonable values. A survey of previous literature found that K''_0 is typically less than 1 GPa^{-1} and always less than ~3 GPa^{-1} (SI Section 3.1). In the fourth-order Birch-Murnaghan fits that properly fit the SBA-15 data, if K'_0 was limited to physically reasonable values then K''_0 fit to >10 GPa^{-1}. Alternatively, if K''_0 was limited to physically reasonable values then K'_0 fit to >10 GPa^{-1}.

EOS Model Approximating the Fused Silica Elastic Anomaly:

Attempts to fit the model approximating the elastic anomaly in fused silica (SI Section 2.6) tested whether a similar phenomenon was taking place in SBA-15. First, we attempted to replicate the SBA-15 data using this model with similar bulk modulus behavior as fused silica (K_0 = 37 GPa, $K'_{Low\text{-}P}$ = -5, $K'_{High\text{-}P}$ = 3.5 [50,65]) but with the elastic anomaly transition $P_{Transition}$ moved to lower or higher pressures. This method cannot replicate the SBA-15 behavior. Similarly, when all the fitting parameters for this model are allowed to vary it is unable to fit the SBA-15 compression data while $K'_{Low\text{-}P}$ and $K'_{High\text{-}P}$ are constrained to physically realistic values. Furthermore, the behavior of the bulk modulus K(P) tries to converge with that from the unphysical third-order Birch-Murnaghan fit. This shows that a sudden change in K' is an especially bad explanation for the SBA-15 EOS data. Thus, the SBA-15 EOS transition is likely mechanistically dissimilar to the elastic anomaly in fused silica. This is further supported by the fact that the FSDP transition is correlated to the EOS transition, which is not seen for the elastic anomaly but commonly observed for LDA-to-HDA transitions.

Appendix C

The position of the FSDP can be converted to a length scale d using $d=(2\pi)/q_{FSDP}$, and if we assume that this length scale corresponds to a spherical scattering structure then we can calculate an "FSDP cell" volume using $V_{FSDP} \propto d^3$ and $V_{FSDP,normalized}=d^3/{d_0}^3$ where d_0 is the FSDP length scale at ambient pressure [56]. The normalized FSDP cell volume can be compared against the normalized bulk *a*SiO_2 volume to compare the "densification" of the FSDP cell with the densification of the bulk.

Figure C.1 compares the volumetric compression of the bulk *a*SiO_2 against the volumetric compression of the FSDP cell for several *a*SiO_2 polyamorphs. The figure shows that polyamorphs with stiffer intertetrahedral networks have more similar bulk and FSDP cell compressibilities. Fused silica with dissolved helium [54], which likely has the stiffest intertetrahedral network due to the "pinning" effect of interstitial helium, has almost no compressibility difference between the bulk and the FSDP cell. Densified fused silica [16], which has a stiffened intertetrahedral network due to reduced interstitial void space, has a small compressibility difference between the bulk and the FSDP cell. Fused silica, which does not have any mechanism to stiffen its intertetrahedral network, has a large compressibility difference between the bulk and the FSDP cell. SBA-15, which likely has increased Si-O-Si bond flexibility due to its nanoscale walls (as discussed in Section 5.5), has the largest compressibility difference between the bulk and the FSDP cell.

[Insert Figure C.1 near here]

References

[1] T. Uchino, Structure and Properties of Amorphous Silica and Its Related Materials: Recent Developments and Future Directions, J. Ceram. Soc. Japan 113 (2005) 17–25. https://doi.org/10.2109/jcersj.113.17.

[2] P.S. Salmon, A. Zeidler, M. Shiga, Y. Onodera, S. Kohara, Ring compaction as a mechanism of densification in amorphous silica, Phys. Rev. B 107 (2023) 144203. https://doi.org/10.1103/PhysRevB.107.144203.

[3] Y. Onodera, S. Kohara, P.S. Salmon, A. Hirata, N. Nishiyama, S. Kitani, A. Zeidler, M. Shiga, A. Masuno, H. Inoue, S. Tahara, A. Polidori, H.E. Fischer, T. Mori, S. Kojima, H. Kawaji, A.I. Kolesnikov, M.B. Stone, M.G. Tucker, M.T. McDonnell, A.C. Hannon, Y. Hiraoka, I. Obayashi, T. Nakamura, J. Akola, Y. Fujii, K. Ohara, T. Taniguchi, O. Sakata, Structure and properties of densified silica glass: characterizing the order within disorder, NPG Asia Mater 12 (2020) 85. https://doi.org/10.1038/s41427-020-00262-z.

[4] Y. Shi, J. Neuefeind, D. Ma, K. Page, L.A. Lamberson, N.J. Smith, A. Tandia, A.P. Song, Ring size distribution in silicate glasses revealed by neutron scattering first sharp diffraction peak analysis, Journal of Non-Crystalline Solids 516 (2019) 71–81. https://doi.org/10.1016/j.jnoncrysol.2019.03.037.

[5] T. Uchino, J.D. Harrop, S.N. Taraskin, S.R. Elliott, Real and reciprocal space structural correlations contributing to the first sharp diffraction peak in silica glass, Phys. Rev. B 71 (2005) 014202. https://doi.org/10.1103/PhysRevB.71.014202.

[6] P.H. Gaskell, D.J. Wallis, Medium-Range Order in Silica, the Canonical Network Glass, Phys. Rev. Lett. 76 (1996) 66–69. https://doi.org/10.1103/PhysRevLett.76.66.

[7] S.R. Elliott, The origin of the first sharp diffraction peak in the structure factor of covalent glasses and liquids, J. Phys.: Condens. Matter 4 (1992) 7661–7678. https://doi.org/10.1088/0953-8984/4/38/003.

[8] Q. Mei, C.J. Benmore, S. Sen, R. Sharma, J.L. Yarger, Intermediate range order in vitreous silica from a partial structure factor analysis, Phys. Rev. B 78 (2008) 144204. https://doi.org/10.1103/PhysRevB.78.144204.

[9] P. Biswas, D. Dahal, S.R. Elliott, New insights into the origin of the first sharp diffraction peak in amorphous silica from an analysis of chemical and radial ordering, (2024). http://arxiv.org/abs/2403.10632 (accessed April 5, 2024).

[10] C. Prescher, V.B. Prakapenka, J. Stefanski, S. Jahn, L.B. Skinner, Y. Wang, Beyond sixfold coordinated Si in SiO2 glass at ultrahigh pressures, Proc. Natl. Acad. Sci. U.S.A. 114 (2017) 10041–10046. https://doi.org/10.1073/pnas.1708882114.

[11] M. Guerette, M.R. Ackerson, J. Thomas, F. Yuan, E. Bruce Watson, D. Walker, L. Huang, Structure and Properties of Silica Glass Densified in Cold Compression and Hot Compression, Sci Rep 5 (2015) 15343. https://doi.org/10.1038/srep15343.

[12] C. Meade, R.J. Hemley, H.K. Mao, High-pressure x-ray diffraction of SiO 2 glass, Phys. Rev. Lett. 69 (1992) 1387–1390. https://doi.org/10.1103/PhysRevLett.69.1387.

[13] T. Uchino, A. Aboshi, T. Yamada, Y. Inamura, Y. Katayama, In situ x-ray diffraction study of the size dependence of pressure-induced structural transformation in

amorphous silica nanoparticles, Phys. Rev. B 77 (2008) 132201. https://doi.org/10.1103/PhysRevB.77.132201.
[14] R. Popescu, M. Zaharescu, A. Vasilescu, G. Catana, R. Manaila, Intermediate-range order in base-catalyzed sol-gel silica, Journal of Non-Crystalline Solids 192–193 (1995) 137–139. https://doi.org/10.1016/0022-3093(95)00341-X.
[15] T. Wakihara, W. Fan, S. Kohara, M. Ogura, G. Sankar, T. Okubo, Intermediate-range Order in Mesoporous Silicas Investigated by a High-energy X-ray Diffraction Technique, Chem. Lett. 37 (2008) 30–31. https://doi.org/10.1246/cl.2008.30.
[16] D. Wakabayashi, N. Funamori, T. Sato, T. Taniguchi, Compression behavior of densified SiO 2 glass, Phys. Rev. B 84 (2011) 144103. https://doi.org/10.1103/PhysRevB.84.144103.
[17] A. Zeidler, P.S. Salmon, L.B. Skinner, Packing and the structural transformations in liquid and amorphous oxides from ambient to extreme conditions, Proc. Natl. Acad. Sci. U.S.A. 111 (2014) 10045–10048. https://doi.org/10.1073/pnas.1405660111.
[18] V. Chaudhary, S. Sharma, An overview of ordered mesoporous material SBA-15: synthesis, functionalization and application in oxidation reactions, J Porous Mater 24 (2017) 741–749. https://doi.org/10.1007/s10934-016-0311-z.
[19] V.L. Zholobenko, A.Y. Khodakov, M. Impéror-Clerc, D. Durand, I. Grillo, Initial stages of SBA-15 synthesis: An overview, Advances in Colloid and Interface Science 142 (2008) 67–74. https://doi.org/10.1016/j.cis.2008.05.003.
[20] D. Zhao, Q. Huo, J. Feng, B.F. Chmelka, G.D. Stucky, Nonionic Triblock and Star Diblock Copolymer and Oligomeric Surfactant Syntheses of Highly Ordered, Hydrothermally Stable, Mesoporous Silica Structures, J. Am. Chem. Soc. 120 (1998) 6024–6036. https://doi.org/10.1021/ja974025i.
[21] D. Zhao, J. Feng, Q. Huo, N. Melosh, G.H. Fredrickson, B.F. Chmelka, G.D. Stucky, Triblock Copolymer Syntheses of Mesoporous Silica with Periodic 50 to 300 Angstrom Pores, Science 279 (1998) 548–552. https://doi.org/10.1126/science.279.5350.548.
[22] G. Chen, C. Wan, Residual strain in thermally annealed periodic mesoporous silica revealed by x-ray scattering, Appl. Phys. Lett. 96 (2010) 141906. https://doi.org/10.1063/1.3380663.
[23] S.M.L. dos Santos, K.A.B. Nogueira, M. de Souza Gama, J.D.F. Lima, I.J. da Silva Júnior, D.C.S. de Azevedo, Synthesis and characterization of ordered mesoporous silica (SBA-15 and SBA-16) for adsorption of biomolecules, Microporous and Mesoporous Materials 180 (2013) 284–292. https://doi.org/10.1016/j.micromeso.2013.06.043.
[24] M. Kruk, M. Jaroniec, C.H. Ko, R. Ryoo, Characterization of the Porous Structure of SBA-15, Chem. Mater. 12 (2000) 1961–1968. https://doi.org/10.1021/cm000164e.
[25] R.A. Pollock, B.R. Walsh, J. Fry, I.T. Ghampson, Y.B. Melnichenko, H. Kaiser, R. Pynn, W.J. DeSisto, M.C. Wheeler, B.G. Frederick, Size and Spatial Distribution of Micropores in SBA-15 using CM-SANS, Chem. Mater. 23 (2011) 3828–3840. https://doi.org/10.1021/cm200707y.
[26] C.J. Gommes, H. Friedrich, M. Wolters, P.E.D. Jongh, K.P.D. Jong, Quantitative Characterization of Pore Corrugation in Ordered Mesoporous Materials Using Image Analysis of Electron Tomograms, Chem. Mater. 21 (2009) 1311–1317. https://doi.org/10.1021/cm803092c.

[27] P. Yuan, L. Tan, D. Pan, Y. Guo, L. Zhou, J. Yang, J. Zou, C. Yu, A systematic study of long-range ordered 3D-SBA-15 materials by electron tomography, New J. Chem. 35 (2011) 2456. https://doi.org/10.1039/c1nj20146h.
[28] J. Rantanen, D. Majda, J. Riikonen, V.-P. Lehto, The atomic local ordering of SBA-15 studied with pair distribution function analysis, and its relationship to porous structure and thermal stability, Acta Materialia 175 (2019) 341–347. https://doi.org/10.1016/j.actamat.2019.06.005.
[29] Y. Borodko, J.W. Ager, G.E. Marti, H. Song, K. Niesz, G.A. Somorjai, Structure Sensitivity of Vibrational Spectra of Mesoporous Silica SBA-15 and Pt/SBA-15, J. Phys. Chem. B 109 (2005) 17386–17390. https://doi.org/10.1021/jp051801x.
[30] L. Jin, S.M. Auerbach, P.A. Monson, Simulating the Formation of Surfactant-Templated Mesoporous Silica Materials: A Model with Both Surfactant Self-Assembly and Silica Polymerization, Langmuir 29 (2013) 766–780. https://doi.org/10.1021/la304475j.
[31] M. Ookawa, Y. Yogoro, T. Yamaguchi, K. Kawamura, X-ray diffraction analysis of ordered mesoporous silica, in: A. Galarneau (Ed.), Zeolites and Mesoporous Materials at the Dawn of the 21st Century: Proceedings of the 13th International Zeolite Conference, Montpellier, France, 8-13 July 2001, 1st ed., Elsevier, Amsterdam ; New York, 2001: p. 198.
[32] D.G. Kizzire, S. Dey, R.A. Mayanovic, R. Sakidja, K. Landskron, M. Mandal, Z. Wang, M. Benamara, Studies of the mechanical and extreme hydrothermal properties of periodic mesoporous silica and aluminosilica materials, Microporous and Mesoporous Materials 252 (2017) 69–78. https://doi.org/10.1016/j.micromeso.2017.06.016.
[33] J. Wu, X. Liu, S.H. Tolbert, High-Pressure Stability in Ordered Mesoporous Silicas: Rigidity and Elasticity through Nanometer Scale Arches, J. Phys. Chem. B 104 (2000) 11837–11841. https://doi.org/10.1021/jp002938k.
[34] R.A. Mayanovic, H. Yan, A.D. Brandt, Z. Wang, M. Mandal, K. Landskron, W.A. Bassett, Mechanical and hydrothermal stability of mesoporous materials at extreme conditions, Microporous and Mesoporous Materials 195 (2014) 161–166. https://doi.org/10.1016/j.micromeso.2014.04.027.
[35] C.C. Liu, G.E. Maciel, The Fumed Silica Surface: A Study by NMR, J. Am. Chem. Soc. 118 (1996) 5103–5119. https://doi.org/10.1021/ja954120w.
[36] C. Martinet, A. Kassir-Bodon, T. Deschamps, A. Cornet, S. Le Floch, V. Martinez, B. Champagnon, Permanently densified SiO_2 glasses: a structural approach, J. Phys.: Condens. Matter 27 (2015) 325401. https://doi.org/10.1088/0953-8984/27/32/325401.
[37] T. Uchino, A. Aboshi, S. Kohara, Y. Ohishi, M. Sakashita, K. Aoki, Microscopic structure of nanometer-sized silica particles, Phys. Rev. B 69 (2004) 155409. https://doi.org/10.1103/PhysRevB.69.155409.
[38] C.J. Benmore, E. Soignard, S.A. Amin, M. Guthrie, S.D. Shastri, P.L. Lee, J.L. Yarger, Structural and topological changes in silica glass at pressure, Phys. Rev. B 81 (2010) 054105. https://doi.org/10.1103/PhysRevB.81.054105.
[39] G. Shen, H.K. Mao, High-pressure studies with x-rays using diamond anvil cells, Rep. Prog. Phys. 80 (2017) 016101. https://doi.org/10.1088/1361-6633/80/1/016101.
[40] S. Klotz, J.-C. Chervin, P. Munsch, G. Le Marchand, Hydrostatic limits of 11 pressure transmitting media, J. Phys. D: Appl. Phys. 42 (2009) 075413. https://doi.org/10.1088/0022-3727/42/7/075413.

[41] C. Prescher, V.B. Prakapenka, DIOPTAS : a program for reduction of two-dimensional X-ray diffraction data and data exploration, High Pressure Research 35 (2015) 223–230. https://doi.org/10.1080/08957959.2015.1059835.
[42] C.J. Gommes, G. Prieto, P.E. De Jongh, Small-Angle Scattering Analysis of Empty or Loaded Hierarchical Porous Materials, J. Phys. Chem. C 120 (2016) 1488–1506. https://doi.org/10.1021/acs.jpcc.5b09556.
[43] S. Förster, A. Timmann, M. Konrad, C. Schellbach, A. Meyer, S.S. Funari, P. Mulvaney, R. Knott, Scattering Curves of Ordered Mesoscopic Materials, J. Phys. Chem. B 109 (2005) 1347–1360. https://doi.org/10.1021/jp0467494.
[44] M. Impéror-Clerc, P. Davidson, A. Davidson, Existence of a Microporous Corona around the Mesopores of Silica-Based SBA-15 Materials Templated by Triblock Copolymers, J. Am. Chem. Soc. 122 (2000) 11925–11933. https://doi.org/10.1021/ja002245h.
[45] B. Hammouda, A new Guinier–Porod model, J Appl Crystallogr 43 (2010) 716–719. https://doi.org/10.1107/S0021889810015773.
[46] F. Birch, Finite Elastic Strain of Cubic Crystals, Phys. Rev. 71 (1947) 809–824. https://doi.org/10.1103/PhysRev.71.809.
[47] T. Katsura, Y. Tange, A Simple Derivation of the Birch–Murnaghan Equations of State (EOSs) and Comparison with EOSs Derived from Other Definitions of Finite Strain, Minerals 9 (2019) 745. https://doi.org/10.3390/min9120745.
[48] O.L. Anderson, D.G. Isaak, S. Yamamoto, Anharmonicity and the equation of state for gold, Journal of Applied Physics 65 (1989) 1534–1543. https://doi.org/10.1063/1.342969.
[49] F.G. Pazzona, B.J. Borah, P. Demontis, G.B. Suffritti, S. Yashonath, A comparative molecular dynamics study of diffusion of n-decane and 3-methyl pentane in Y zeolite, J Chem Sci 121 (2009) 921–927. https://doi.org/10.1007/s12039-009-0109-5.
[50] C. Meade, R. Jeanloz, Frequency-dependent equation of state of fused silica to 10 GPa, Phys. Rev. B 35 (1987) 236–244. https://doi.org/10.1103/PhysRevB.35.236.
[51] B.P. Singh, A comparison of equations of state including the generalized Rydberg EOS, Physica B: Condensed Matter 369 (2005) 111–116. https://doi.org/10.1016/j.physb.2005.08.004.
[52] X. Hong, G. Shen, V.B. Prakapenka, M. Newville, M.L. Rivers, S.R. Sutton, Intermediate states of GeO2 glass under pressures up to 35 GPa, Phys. Rev. B 75 (2007) 104201. https://doi.org/10.1103/PhysRevB.75.104201.
[53] M. Bull, R. Huber, P. Yu, T. Finney, N. Felvey, P. Chow, Y. Xiao, T. Kuhl, E. Watkins, In-situ SAXS and XRD of SBA-15 in a Diamond Anvil Cell during high-pressure densification [dataset], (2024). https://doi.org/10.17632/4SNCVXBN6X.1.
[54] T. Sato, N. Funamori, T. Yagi, Helium penetrates into silica glass and reduces its compressibility, Nat Commun 2 (2011) 345. https://doi.org/10.1038/ncomms1343.
[55] T. Sato, N. Funamori, High-pressure in situ density measurement of low-Z noncrystalline materials with a diamond-anvil cell by an x-ray absorption method, Review of Scientific Instruments 79 (2008) 073906. https://doi.org/10.1063/1.2953093.
[56] C.Z. Tan, J. Arndt, X-ray diffraction of densified silica glass, (1999).
[57] D.C. Hannah, J. Yang, P. Podsiadlo, M.K.Y. Chan, A. Demortière, D.J. Gosztola, V.B. Prakapenka, G.C. Schatz, U. Kortshagen, R.D. Schaller, On the Origin of Photoluminescence in Silicon Nanocrystals: Pressure-Dependent Structural and

Optical Studies, Nano Lett. 12 (2012) 4200–4205. https://doi.org/10.1021/nl301787g.
[58] V. Swamy, L.S. Dubrovinsky, N.A. Dubrovinskaia, A.S. Simionovici, M. Drakopoulos, V. Dmitriev, H.-P. Weber, Compression behavior of nanocrystalline anatase TiO2, Solid State Communications 125 (2003) 111–115. https://doi.org/10.1016/S0038-1098(02)00601-4.
[59] S.B. Qadri, E.F. Skelton, A.D. Dinsmore, J.Z. Hu, W.J. Kim, C. Nelson, B.R. Ratna, The effect of particle size on the structural transitions in zinc sulfide, Journal of Applied Physics 89 (2001) 115–119. https://doi.org/10.1063/1.1328066.
[60] J. Haines, O. Cambon, C. Levelut, M. Santoro, F. Gorelli, G. Garbarino, Deactivation of Pressure-Induced Amorphization in Silicalite SiO_2 by Insertion of Guest Species, J. Am. Chem. Soc. 132 (2010) 8860–8861. https://doi.org/10.1021/ja1034599.
[61] J.B. Walsh, First Pressure Derivative of Bulk Modulus for Porous Materials, Journal of Applied Physics 42 (1971) 1098–1100. https://doi.org/10.1063/1.1660150.
[62] S. Susman, K.J. Volin, D.L. Price, M. Grimsditch, J.P. Rino, R.K. Kalia, P. Vashishta, G. Gwanmesia, Y. Wang, R.C. Liebermann, Intermediate-range order in permanently densified vitreous SiO 2 : A neutron-diffraction and molecular-dynamics study, Phys. Rev. B 43 (1991) 1194–1197. https://doi.org/10.1103/PhysRevB.43.1194.
[63] A. Zeidler, K. Wezka, R.F. Rowlands, D.A.J. Whittaker, P.S. Salmon, A. Polidori, J.W.E. Drewitt, S. Klotz, H.E. Fischer, M.C. Wilding, C.L. Bull, M.G. Tucker, M. Wilson, High-Pressure Transformation of SiO 2 Glass from a Tetrahedral to an Octahedral Network: A Joint Approach Using Neutron Diffraction and Molecular Dynamics, Phys. Rev. Lett. 113 (2014) 135501. https://doi.org/10.1103/PhysRevLett.113.135501.
[64] C. Zha, R.J. Hemley, H. Mao, T.S. Duffy, C. Meade, Acoustic velocities and refractive index of SiO 2 glass to 57.5 GPa by Brillouin scattering, Phys. Rev. B 50 (1994) 13105–13112. https://doi.org/10.1103/PhysRevB.50.13105.
[65] K. Suito, M. Miyoshi, T. Sasakurau, H. Fujisawa, Elastic Properties of Obsidian, Vitreous SiO_2 , and Vitreous GeO_2 under High Pressure up to 6 GPa, in: Y. Syono, M.H. Manghnani (Eds.), Geophysical Monograph Series, American Geophysical Union, Washington, D. C., 1992: pp. 219–225. https://doi.org/10.1029/GM067p0219.
[66] L. Huang, J. Kieffer, Amorphous-amorphous transitions in silica glass. I. Reversible transitions and thermomechanical anomalies, Phys. Rev. B 69 (2004) 224203. https://doi.org/10.1103/PhysRevB.69.224203.
[67] C. Weigel, M. Foret, B. Hehlen, M. Kint, S. Clément, A. Polian, R. Vacher, B. Rufflé, Polarized Raman spectroscopy of v − SiO 2 under rare-gas compression, Phys. Rev. B 93 (2016) 224303. https://doi.org/10.1103/PhysRevB.93.224303.
[68] T. Uchino, A. Sakoh, M. Azuma, S. Kohara, M. Takahashi, M. Takano, T. Yoko, Anelastic compression of nanometer-sized silica particles under high pressure: A high-energy x-ray diffraction measurement, Phys. Rev. B 67 (2003) 092202. https://doi.org/10.1103/PhysRevB.67.092202.
[69] T. Sakamaki, Y. Kono, Y. Wang, C. Park, T. Yu, Z. Jing, G. Shen, Contrasting sound velocity and intermediate-range structural order between polymerized and depolymerized silicate glasses under pressure, Earth and Planetary Science Letters 391 (2014) 288–295. https://doi.org/10.1016/j.epsl.2014.02.008.

[70] T. Deschamps, J. Margueritat, C. Martinet, A. Mermet, B. Champagnon, Elastic Moduli of Permanently Densified Silica Glasses, Sci Rep 4 (2014) 7193. https://doi.org/10.1038/srep07193.
[71] T. Uchino, A. Sakoh, M. Azuma, M. Takano, M. Takahashi, T. Yoko, A novel pressure-induced polymorphic transition from fumed silica to transparent amorphous SiO_2 at room temperature, J. Phys.: Condens. Matter 14 (2002) 11111–11114. https://doi.org/10.1088/0953-8984/14/44/434.
[72] J.Z. Jiang, J.S. Olsen, L. Gerward, S. Mørup, Enhanced bulk modulus and reduced transition pressure in γ-Fe2O3 nanocrystals, Europhys. Lett. 44 (1998) 620–626. https://doi.org/10.1209/epl/i1998-00563-6.
[73] Z. Wang, S.K. Saxena, V. Pischedda, H.P. Liermann, C.S. Zha, X-ray diffraction study on pressure-induced phase transformations in nanocrystalline anatase/rutile (TiO_2), J. Phys.: Condens. Matter 13 (2001) 8317–8323. https://doi.org/10.1088/0953-8984/13/36/307.
[74] Z. Wang, S.K. Saxena, V. Pischedda, H.P. Liermann, C.S. Zha, *In situ* x-ray diffraction study of the pressure-induced phase transformation in nanocrystalline CeO 2, Phys. Rev. B 64 (2001) 012102. https://doi.org/10.1103/PhysRevB.64.012102.
[75] X. Dong, H. Liu, J. Hou, K. Wu, Z. Chen, Phase Equilibria of Confined Fluids in Nanopores of Tight and Shale Rocks Considering the Effect of Capillary Pressure and Adsorption Film, Ind. Eng. Chem. Res. 55 (2016) 798–811. https://doi.org/10.1021/acs.iecr.5b04276.
[76] K. Zhang, N. Jia, L. Liu, Adsorption Thicknesses of Confined Pure and Mixing Fluids in Nanopores, Langmuir 34 (2018) 12815–12826. https://doi.org/10.1021/acs.langmuir.8b02925.
[77] J. Haines, C. Levelut, A. Isambert, P. Hébert, S. Kohara, D.A. Keen, T. Hammouda, D. Andrault, Topologically Ordered Amorphous Silica Obtained from the Collapsed Siliceous Zeolite, Silicalite-1-F: A Step toward “Perfect” Glasses, J. Am. Chem. Soc. 131 (2009) 12333–12338. https://doi.org/10.1021/ja904054v.
[78] M.T. Wharmby, F. Niekiel, J. Benecke, S. Waitschat, H. Reinsch, D. Daisenberger, N. Stock, P.G. Yot, Influence of Thermal and Mechanical Stimuli on the Behavior of Al-CAU-13 Metal–Organic Framework, Nanomaterials 10 (2020) 1698. https://doi.org/10.3390/nano10091698.
[79] K.W. Chapman, G.J. Halder, P.J. Chupas, Guest-Dependent High Pressure Phenomena in a Nanoporous Metal−Organic Framework Material, J. Am. Chem. Soc. 130 (2008) 10524–10526. https://doi.org/10.1021/ja804079z.
[80] A. Półrolniczak, S. Sobczak, V.I. Nikolayenko, L.J. Barbour, A. Katrusiak, Solvent-controlled elongation and mechanochemical strain in a metal–organic framework, Dalton Trans. 50 (2021) 17478–17481. https://doi.org/10.1039/D1DT01937F.
[81] Y.V. Seryotkin, Evolution of the brewsterite structure at high pressure: A single-crystal X-ray diffraction study, Microporous and Mesoporous Materials 276 (2019) 167–172. https://doi.org/10.1016/j.micromeso.2018.09.030.
[82] H. Wu, Z. Wang, H. Fan, Stress-Induced Nanoparticle Crystallization, J. Am. Chem. Soc. 136 (2014) 7634–7636. https://doi.org/10.1021/ja503320s.
[83] P. Podsiadlo, B. Lee, V.B. Prakapenka, G.V. Krylova, R.D. Schaller, A. Demortière, E.V. Shevchenko, High-Pressure Structural Stability and Elasticity of Supercrystals Self-Assembled from Nanocrystals, Nano Lett. 11 (2011) 579–588. https://doi.org/10.1021/nl103587u.

[84] Y. Inamura, Y. Katayama, W. Utsumi, K. Funakoshi, Transformations in the Intermediate-Range Structure of SiO2 Glass under High Pressure and Temperature, Phys. Rev. Lett. 93 (2004) 015501. https://doi.org/10.1103/PhysRevLett.93.015501.
[85] N. Funamori, T. Sato, A cubic boron nitride gasket for diamond-anvil experiments, Review of Scientific Instruments 79 (2008) 053903. https://doi.org/10.1063/1.2917409.
[86] T. Sato, N. Funamori, High-pressure *in situ* density measurement of low-Z noncrystalline materials with a diamond-anvil cell by an x-ray absorption method, Review of Scientific Instruments 79 (2008) 073906. https://doi.org/10.1063/1.2953093.

Figures

Figure 1a

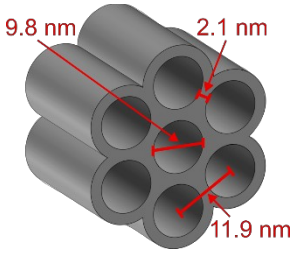

Figure 1b

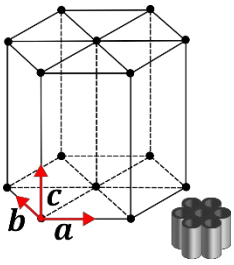

Figure 2

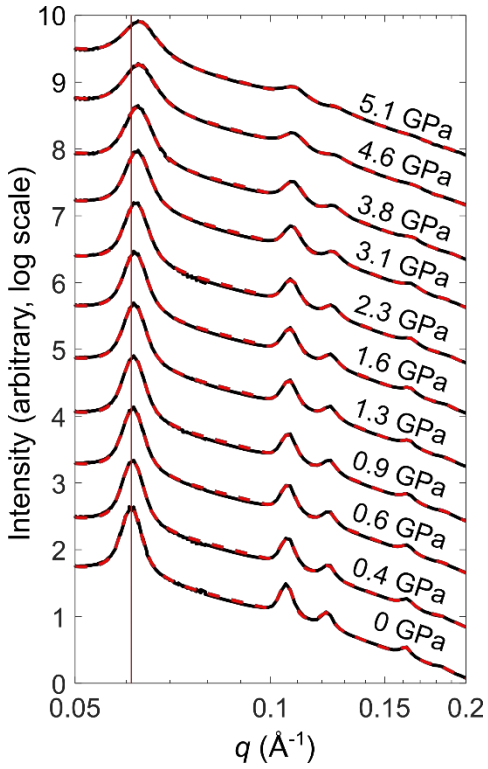
Intensity (arbitrary, log scale)
q (Å-1)
5.1 GPa
4.6 GPa
3.8 GPa
3.1 GPa
2.3 GPa
1.6 GPa
1.3 GPa
0.9 GPa
0.6 GPa
0.4 GPa
0 GPa
0
1
2
3
4
5
6
7
8
9
10
0.05
0.1
0.15
0.2

Figure 3

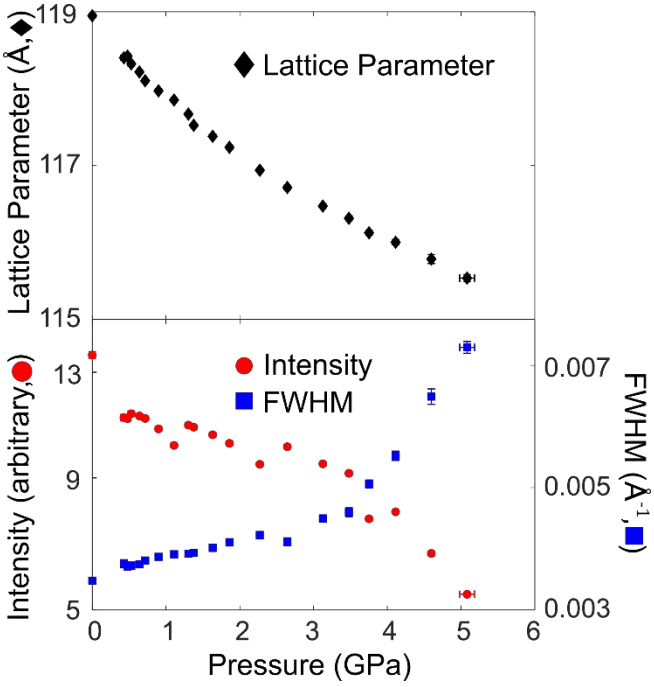
Lattice Parameter (Å,◆)
119
117
115
Lattice Parameter
Intensity (arbitrary,●)
13
9
5
Intensity
FWHM
0.007
0.005
0.003
FWHM (Å-1,■)
0
1
2
3
4
5
6
Pressure (GPa)

Figure 4

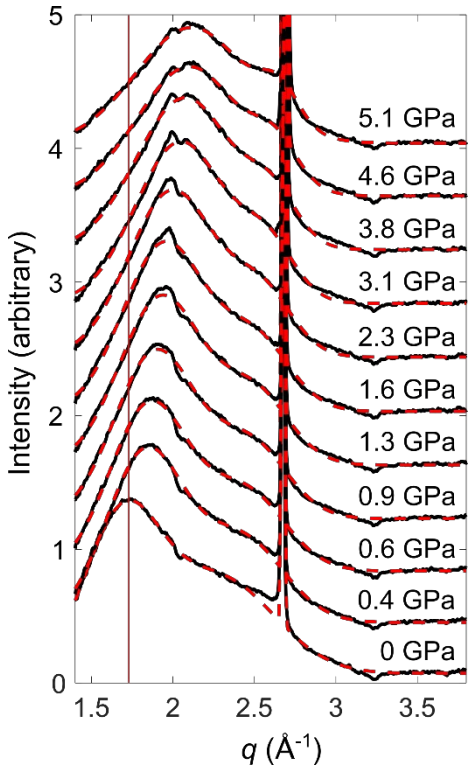
5.1 GPa
4.6 GPa
3.8 GPa
3.1 GPa
2.3 GPa
1.6 GPa
1.3 GPa
0.9 GPa
0.6 GPa
0.4 GPa
0 GPa
Intensity (arbitrary)
q (Å-1)
0
1
2
3
4
5
1.5
2
2.5
3
3.5

1173 Figure 5

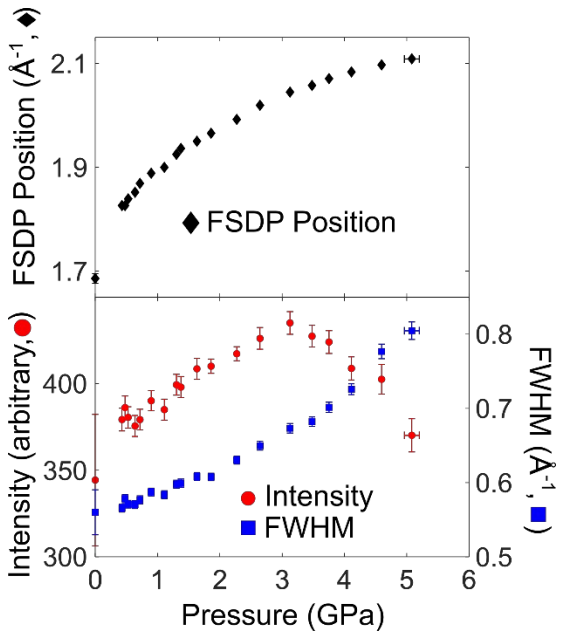

1174

1175

1176 Figure 6

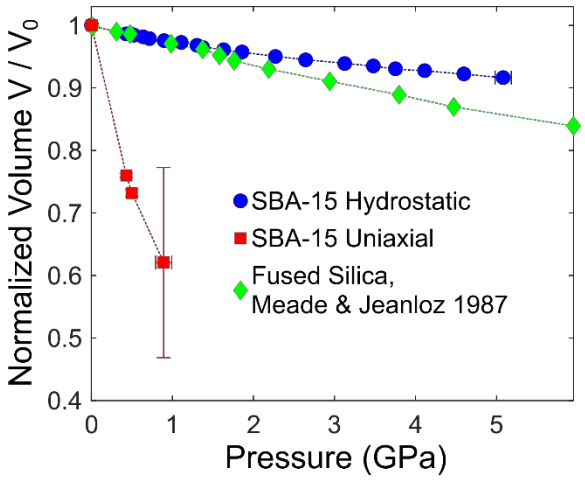

1177

1178

1179 Figure 7

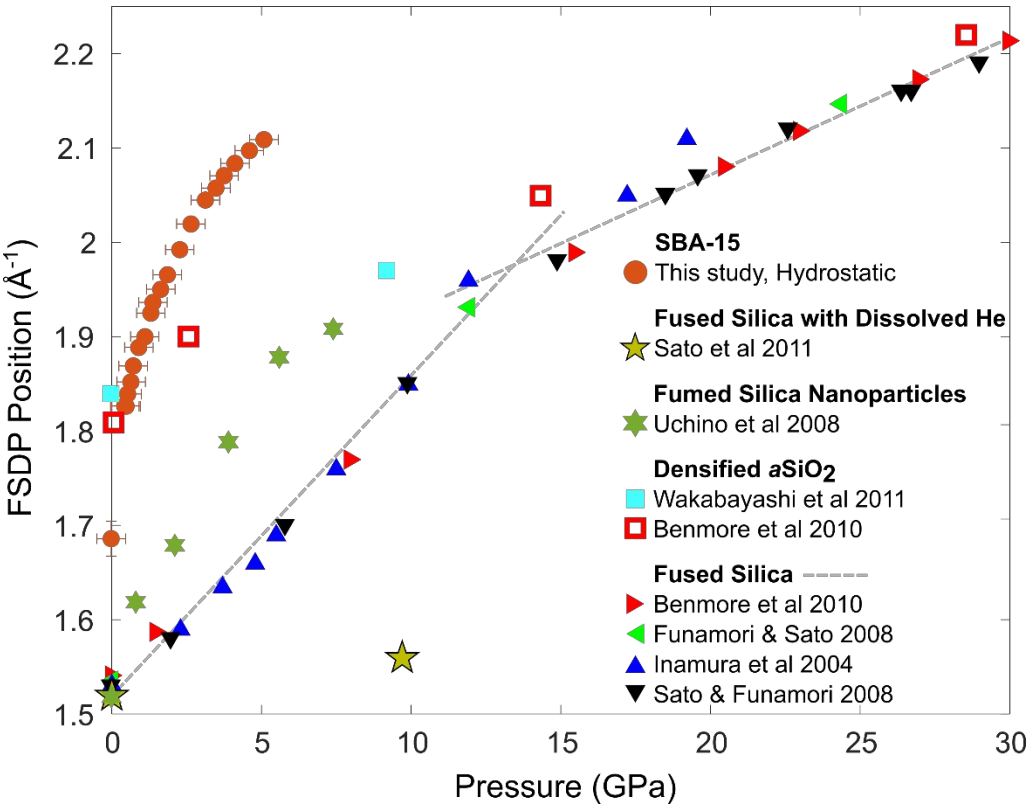

1180

1181

1182 Figure 8

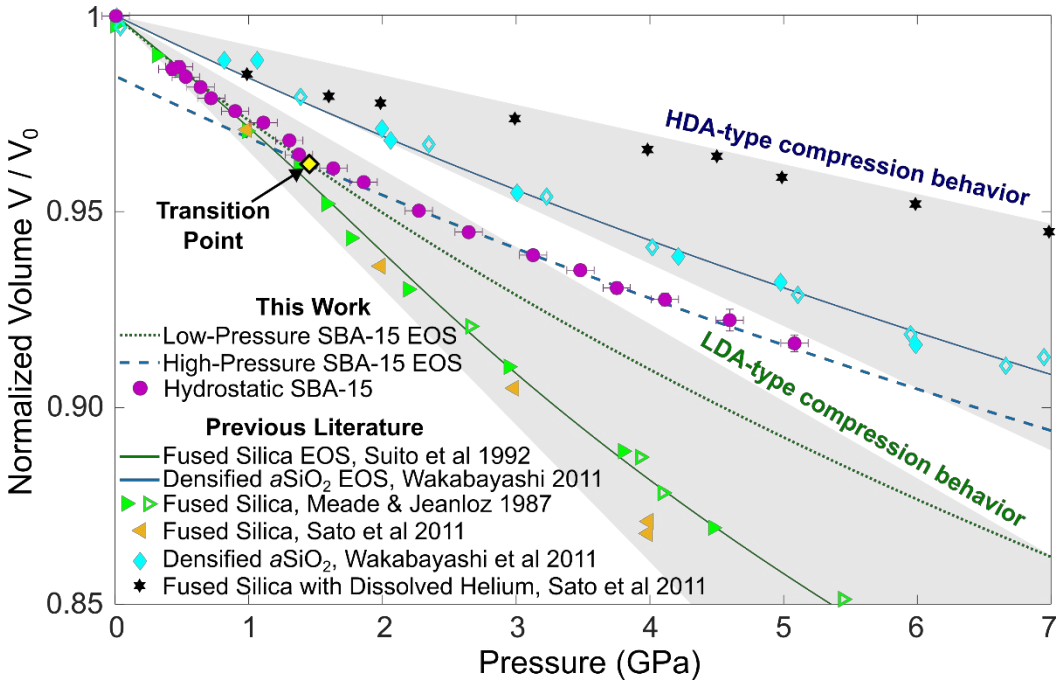

1183

1184

1185 Figure C.1

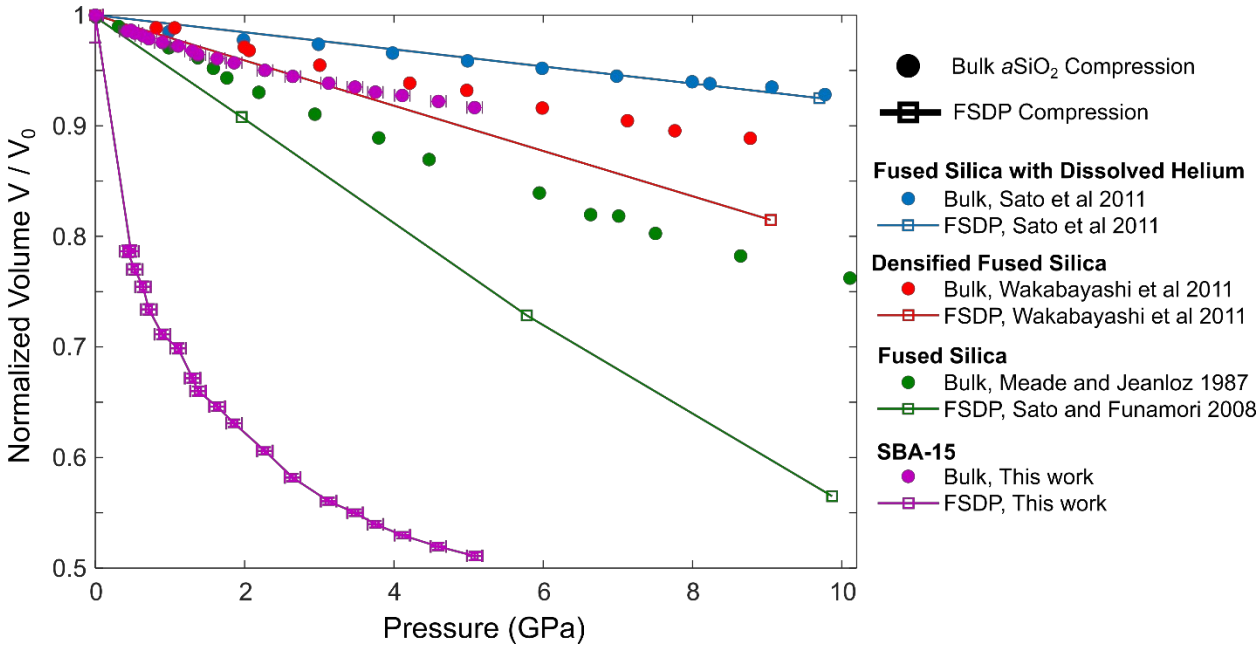

1186

1187

Figure Captions

Figure 1: (a) Schematic of SBA-15 honeycomb structure. Cylindrical mesopores are arranged within an *a*SiO_2 matrix which forms thin walls between the them. Although schematically shown as smooth and solid, the aSiO2 walls are rough and have a high intrawall void fraction [25]. The primary mesopores have diameters of 9.8 nm and the minimum wall thickness is ~2.1 nm. (b) The hexagonal *P*6*mm* mesolattice in SBA-15. Each vertical line represents the center of a mesopore. Crystallographic directions are shown as red vectors. Because the lattice is 2D, the lattice parameter in the *c*-direction is essentially infinite. For a *P*6*mm* lattice, the parameters in the *a*- and *b*-crystallographic directions are equivalent (11.9 nm).

Figure 2: Hydrostatic compression of SBA-15 measured using SAXS. Black lines are SAXS data, red dashed lines are model fits to the data. Data is offset for clarity. The vertical light red line illustrates the shift in the low-*q* peak with pressure.

Figure 3: SBA-15 mesopore lattice parameter α calculated from the *q* positions of the SAXS diffraction peaks (black diamonds), and SAXS (10) reflection integrated peak intensity (red circles) and FWHM (blue squares) for hydrostatically compressed SBA-15 as a function of pressure. At ~3 – 4 GPa there is an inflection in the pressure dependence of the intensity and FWHM, but not for the lattice parameter. Vertical error bars are shown, but mostly smaller than the datapoints. Representative errors in pressure are shown on the final symbol of each dataset.

Figure 4: XRD data of SBA-15 under hydrostatic compression. Black lines are XRD data, red dashed lines are model fits to the data. Porod and constant background components have been subtracted and the data is shifted vertically for clarity. The vertical feature near $q \approx 2.6$ Å^{-1} is the gold (111) reflection. The oscillation occurring in all datasets around $q \approx 2$ Å^{-1} is a detector masking artifact. The vertical light red line illustrates the shift in the FSDP with pressure.

Figure 5: Position (black diamonds), Integrated peak intensity (red circles) and FWHM (blue squares) of the low-*q* component of the FSDP peak for SBA-15 during hydrostatic compression. At ~3 GPa there is an inflection point in the intensity. Vertical error bars are shown, but mostly smaller than the symbols. Representative errors in pressure are shown on the final symbol of each dataset.

Figure 6: Comparison of the hydrostatic compression behaviors of SBA-15 with and without a hydrostatic PTM. Fused silica [50] is shown as a benchmark for comparison. Points without visible vertical error bars have errors smaller than their symbols. Representative errors in pressure are shown on the final symbol of each SBA-15 dataset.

Figure 7: Pressure dependence of the FSDP position for different types of amorphous silica [13,16,38,54,55,84,85]. Dotted lines approximate the fused silica low- and high-pressure FSDP regimes. Below ~4 GPa, SBA-15's FSDP position shows a stronger pressure dependence than any previously studied *a*SiO_2 polyamorph. Fumed silica is the only other polyamorph to have an FSDP position with a stronger pressure dependence than fused silica. The SBA-15 FSDP undergoes a transition from strong-to-weak pressure dependence by ~3 GPa, analogous to the FSDP behavior of fused silica at ~13 GPa. After the transition, the FSDP pressure dependence is comparable to stiff *a*SiO_2 polyamorphs like fully densified *a*SiO_2. All points represent compression data except for the unfilled red squares which correspond to decompression of densified fused silica. SBA-15 datapoints with FSDP position errorbars smaller than their symbols have $\sigma_{FSDP} \approx 0.002$ Å^{-1}.

Figure 8: The densification of different polyamorphs of amorphous silica, plotted as a function of normalized volume [16,50,54]. Filled points represent compression, and unfilled points represent decompression. The different compression behaviors can be separated into two major groups: LDA-type behavior and HDA-type behavior. SBA-15 is shown to transition from LDA- to HDA-type behavior at ~2 GPa. SBA-15 datapoints with volume errorbars smaller than their symbols have $\sigma_{V/V0} \approx 0.0015$.

Figure C.1: Comparison between the volumetric compression of the bulk material and the FSDP cell for fused silica with dissolved helium [54], densified fused silica [16], fused silica [50,86], and SBA-15 (this work). Filled circles represent the compression of bulk *a*SiO_2, lines with squares represent the compression of the FSDP cell.